Comparative Assessment of the Harmonic Balance Navier Stokes Technology for Horizontal and Vertical Axis Wind turbine Aerodynamics

M. Sergio Campobasso[a,*], Jernej Drofelnik[b], Fabio Gigante[b]

[a] *University of Lancaster, Department of Engineering. Engineering Building, Gillow Avenue, Lancaster LA1 4YW, United Kingdom.*
[b] *University of Glasgow, School of Engineering. James Watt Building South, University Avenue, Glasgow G12 8QQ, United Kingdom.*

Abstract

Several important wind turbine unsteady flow regimes, such as those associated with the yawed wind condition of horizontal axis machines, and most operating conditions of all vertical axis machines, are predominantly periodic. The harmonic balance Reynolds-averaged Navier-Stokes technology for the rapid calculation of nonlinear periodic flow fields has been successfully used to greatly reduce runtimes of turbomachinery periodic flow analyses in the past fifteen years. This paper presents an objective comparative study of the performance and solution accuracy of this technology for aerodynamic analysis and design applications of horizontal and vertical axis wind turbines. The considered use cases are the periodic flow past the blade section of a utility-scale horizontal axis wind turbine rotor in yawed wind, and the periodic flow of a H-Darrieus rotor section working at a tip-speed ratio close to that of maximum power. The aforementioned comparative assessment is based on thorough parametric time-domain and harmonic balance analyses of both use cases. The paper also reports the main mathematical and numerical features of a new turbulent harmonic balance Navier-Stokes solver using Menter's shear stress transport model for the turbulence closure. Presented results indicate that *a*) typical multimegawatt

*Corresponding author
Email address: `m.s.campobasso@lancaster.ac.uk` (M. Sergio Campobasso)

horizontal axis wind turbine periodic flows can be computed by the harmonic balance solver about ten times more rapidly than by the conventional time-domain analysis, achieving the same temporal accuracy of the latter method, and b) the harmonic balance acceleration for Darrieus rotor unsteady flow analysis is lower than for horizontal axis machines, and the harmonic balance solutions feature undesired oscillations caused by the wide harmonic content and the high-level of stall predisposition of this flow field type.

Keywords: Horizontal and vertical axis wind turbine periodic aerodynamics, Dynamic stall, Harmonic balance Navier-Stokes equations, Shear stress transport turbulence model, Fully coupled multigrid integration, Point-implicit Runge-Kutta smoother

---

Nomenclature

Acronyms

AoA Angle of attack

BEMT Blade element momentum theory

FERK Fully explicit Runge-Kutta

HAWT Horizontal axis wind turbine

HB Harmonic balance

IRS Implicit residual smoothing

MG Multigrid

NS Navier-Stokes

PDE Partial differential equation

PIRK Point-implicit RK

RK Runge-Kutta

TD Time-domain

VAWT Vertical axis wind turbine

Greek symbols

$\Delta\tau$ Pseudo-time-step (s)

Δl_r Logarithm in base 10 of normalized residual RMS of RANS equations

Ω Rotor angular speed (RPM)

Ω_f Flow vorticity (s^{-1})

$\underline{\mathbf{\Phi}}_c$ Generalized steady and TD convective flux vector

$\underline{\mathbf{\Phi}}_{cH}$ Generalized HB convective flux vector

$\underline{\mathbf{\Phi}}_d$ Generalized steady and TD diffusive flux vector

$\underline{\mathbf{\Phi}}_{dH}$ Generalized HB diffusive flux vector

α_∞ Angle of attack associated with velocity vector $\underline{W}_\infty$ ($^\circ$)

α_m m^{th} RK coefficient

δ Yaw angle ($^\circ$)

γ_p Twist angle ($^\circ$)

λ Reduced frequency

λ_D Tip-speed ratio

μ_T Turbulent viscosity (kg/ms)

ν Molecular kinematic viscosity (m^2/s)

ω Specific turbulence dissipation rate (s^{-1})

ϕ^r_∞ Angle of attack associated with velocity vector $\underline{W}^r_\infty$ ($^\circ$)

ρ Density (kg/m^3)

τ_w Wall viscous stress (Pa)

θ VAWT rotor azimuthal position ($^\circ$)

Latin symbols

A Matrix for implicit update of k and ω

CD_ω Cross-diffusion term of ω equation (kg/m^3s^2)

C_l, C_d Lift and drag force coefficients

C'_m Constant-head pitching moment coefficient

C_m Variable-head pitching moment coefficient

C_{MG} Overhead of HB MG cycle

C_T Torque coefficient

C_x, C_y Horizontal and vertical force coefficients

D HB antisymmetric matrix

D_ω Destruction term of ω rate (kg/m^3s^2)

D_k Destruction term of k (kg/ms^3)

M_∞^r Mach number associated with velocity $\underline{W}_\infty^r$

N_H Number of complex harmonics

N_{pde} Number of PDEs

P_d Turbulent production term (s^{-2})

$\mathbf{Q}$ Array of steady and TD conservative variables at cell center

$\mathbf{Q}_H$ Array of HB conservative variables at cell center

R HAWT rotor radius (m)

$\mathbf{R}_\Phi$ Array of steady and TD cell residuals

$\mathbf{R}_{\Phi H}$ Array of HB cell residuals

R_D Darrieus turbine rotor radius (mm)

$\mathbf{R}_{gH}$ Array of HB cell residuals including HB source term

$\mathbf{S}$ Source term of steady and TD equations

$\mathbf{S}_H$ Source term of HB equations

S_k Source term of k equation (kg/ms^3)

S_ω Source term of ω equation (kg/m^3s^2)

T Period (s)

$\mathbf{U}$ Array of steady and TD conservative variables

$\mathbf{U}_H$ Array of HB conservative variables

V_∞ Freestream velocity ahead of HAWT rotor (m/s)

$\underline{W}_\infty$ Absolute freestream velocity vector (m/s)

$\underline{W}_\infty^r$ Relative freestream velocity vector (m/s)

c Chord (m)

c_f, c_p Skin friction and static pressure coefficients

k Turbulent kinetic energy (m^2/s^2)

l RK cycle counter

l_k User-given constant of turbulent production limiters

m RK stage index

p Static pressure (Pa)

p_w Wall static pressure (Pa)

$\underline{\underline{s}}$ Strain rate tensor (s^{-1})

t_n HB snapshot times

$\underline{\mathrm{v}}$ Local absolute velocity vector (m/s)

x_a Airfoil chorswise position (m)

y^+ Dimensionless wall distance

1. Introduction

The aeromechanical design of wind turbines is a complex multidisciplinary task that requires consideration of a very large number of operating regimes due to the extreme variability of the environmental conditions on time scales ranging from seconds (*e.g.* wind gusts) to months (*e.g.* seasonal wind variations). Several fatigue-inducing unsteady regimes, however, are predominantly periodic. In the case of utility-scale horizontal axis wind turbines (HAWTs), periodic fluid-induced excitations of the rotor blades and drivetrain may result from the blades rotating *a*) through wind stratifications associated with the atmospheric boundary layer, *b*) through the variable pressure field due to the presence of the tower (multimegawatt turbines typically feature upwind rotors), *c*) through portions of the wake shed by an upstream turbine in the wind farm environment, *d*) in yawed wind, a condition occurring when the freestream wind velocity is not orthogonal to the turbine rotor [1], and *e*) in a region of nonuniform wind resulting from the combination of two or more of the kind of phenomena mentioned above. With regard to yaw misalignments, utility-scale HAWTs typically feature yaw control systems that monitor the direction of the wind and rotate the entire nacelle towards the wind [2]. However, yaw actuators adjust the nacelle position only after a yaw error has been detected for a relatively long time-interval, usually 10 minutes. Therefore, at sites with frequent variations of the wind direction, blade and drivetrain fatigue due to yawed wind can be significant. HAWT rotors experience constant periodic excitations when the turbines are placed at inclined sites, such as mountainous terrains. Here wind speeds are often higher than on flat terrain due to the acceleration induced by the surface geometry, however the entire wind stream is inclined on the ground, and this yields periodic rotor flows similar to those induced by yaw errors [3]. In all these cases, the fundamental frequency of the periodic excitation is a multiple of the rotor speed.

The flow field past vertical axis wind turbines (VAWTs) [2], such as the popular Darrieus turbine, is inherently unsteady and predominantly periodic in the vast majority of operating conditions. At present these machines are used predominantly for distributed power generation in the built environment. For this application, they are often preferred to HAWTs due their simpler build, simpler and cheaper maintenance requirements, and for their insensitivity to the wind direction. This feature is particularly important in the urban environment, as the variability of wind speed and direction is higher that on open terrains. The Darrieus VAWT is a lift-driven machine in which the blade airfoils are contained and rotate in planes orthogonal to the rotor axis. The periodic nature of the flow past the blades is due to the cyclic variation (every rotor revolution) of modulus and direction of the relative velocity perceived by their airfoils [4], and also the interactions between the blades traveling in the downwind region of the rotor and the vorticity shed by the blades in the upwind rotor region [5]. These complex unsteady flow patterns are further complicated by the occurrence of dynamic stall [6] over a significant portion of the entire turbine operating range [5].

The comments above highlight the necessity of accurately predicting periodic flows when designing wind turbines. This is of crucial importance for reliably predicting the actual amount of harvested energy and the fatigue-inducing loads which may reduce turbine life and/or increase its operation and maintenance costs. In many cases, however, wind turbine design methods still rely on low-fidelity and/or semi-empirical models such as blade element momentum theory (BEMT) and dynamic stall models [7, 8, 9]. The main advantage of these techniques is their extremely high computational speed. Their main drawback is that they heavily rely on the existence and availability of high-quality airfoil data, and this hinders their applicability to the design of radically new turbine configurations. Moreover these low-fidelity methods model strongly unsteady three-dimensional (3D) flow features, such as HAWT yawed flows and the radial pumping effect occurring in the presence of stalled flow [10] with a high degree of uncertainty even when detailed airfoil data are available. A wider discussion on the predictive reliability of low-fidelity tools for the wind turbine design can be found in [11].

The use of high-fidelity computational aerodynamics tools such as Navier-Stokes (NS) Computational Fluid Dynamics (CFD) codes has the potential of greatly reducing the uncertainty associated with the flow predictions of low-fidelity models. Several remarkable examples of the predictive capabilities of NS CFD for HAWT yawed flows have been published, including the articles [12, 13, 14, 15]. The article [12] also includes comparisons of CFD NS results, experimental data and results obtained with low-fidelity codes, including a BEMT code. The report shows that the agreement between NS CFD analysis and measured data is substantially better than that between low-fidelity analyses and measured data, as expected. Early assessments of the NS CFD technology for Darrieus rotor aerodynamics, aiming primarily at thoroughly investigating the complex fluid mechanics of these machines, include the articles [16, 5, 6]. The computational and experimental study reported in [17] provides detailed evidence of the predictive capabilities of 3D NS CFD for Darrieus rotors. An exhaustive comparative assessment of NS CFD and BEMT results, highlighting the difficulties of the BEMT technology of accurately predicting complex flow features, particularly in the absence of reliable airfoil force data, is reported in [18]. The article [19] also highlights that NS codes can predict fairly accurately measured Darrieus turbine aerodynamics provided that best practice in defining the physical domain, constructing the computational grid, and setting up important parameters of the simulation is adopted.

The main drawback of NS simulations is their high computational cost. A fully time-resolved time-domain (TD) NS simulation of wind turbine periodic flows requires a long runtime because several rotor revolutions have to be simulated before the periodic state of interest is achieved. This runtime could be reduced by using a frequency-domain formulation and solution of the governing unsteady equations. The harmonic balance (HB) NS technology for the solution of unsteady periodic flows [20] is one of the most popular technologies of this type. This method has been successfully applied to the prediction of the periodic flow associated with flutter and forced response of turbomachinery blades [20, 21, 22], and various vibratory motion modes of aircraft configurations [23, 24, 25]. For this type of application, the use of the HB NS approach for the calculation of periodic flows can lead to runtime reductions varying between one and two orders of magnitude with respect to conventional TD NS analyses. Other successful nonlinear frequency-domain NS methods exist and have been used, and more detail on this aspect can be found in [26].

A preliminary investigation into the use of the HB NS technology for reducing the analysis runtime of the periodic flow field past HAWT rotor blade sections was reported in [26]. This study was based on the compressible laminar NS equations and used low-speed preconditioning to handle the numerical difficulties resulting from the typically low speeds of wind turbine flows. More realistic turbulent flow demonstrations of this technology for HAWT turbulent aerodynamics have followed, including the study in [27] making use of the one-equation Spalart-Allmaras turbulence model [28], that in [29] making use of the Spalart-Allmaras model and a zonal transition model, and that in [11] making use of Menter's two-equation shear stress transport (SST) turbulence model [30]. The only reported study on the use of the NS HB technology for VAWT aerodynamics is, to the best of the authors' knowledge, the article [31], which presents parametric design studies of a one-blade Darrieus rotor based on a HB NS code making use of an algebraic model for the turbulence closure. These studies indicate a growth in the use of this high-fidelity approach for the analysis of HAWT periodic aerodynamics. However, quantitative measures of the actual benefits of using turbulent HB NS solvers for wind turbine design are still scarce. More specifically, by which amount can a turbulent HB NS code reduce the analysis runtime of wind turbine periodic flows while maintaining a prediction accuracy comparable to that of the corresponding TD code? Can both HAWT and Darrieus VAWT flows be solved with an accuracy comparable to that of the TD method, but more rapidly? The main objective of this paper is to provide a significant contribution to answering these questions.

After presenting the TD and HB integral form of the Reynolds-averaged Navier-Stokes (RANS) equations and the SST turbulence model used for the turbulence closure (section 2), brief descriptions of the multigrid smoother of the steady and HB solvers of the COSA NS research code are provided (section 3). Here emphasis is put on the strongly coupled integration approach of all COSA solvers, which advance concurrently in the integration process the solution of the two systems of algebraic equations resulting from the discretization of the RANS and SST equations. Section 4 considers the periodic flow past the blade section of a utility-scale HAWT. In addition to providing a detailed aerodynamic discussion of this flow problem, time refinement analyses with the TD solver and spectral refinement analyses with the HB solver are performed to determine the speed-up of the HB simulation yielding a solution accuracy comparable to that of the fully resolved TD simulation. The same type of analyses for the periodic flow of a three-blade H-Darrieus rotor section are presented in section 5. The paper is concluded by a summary of the presented analyses and a some perspectives on the future use of the HB NS technology for wind turbine aerodynamics.

2. Governing equations

2.1. Time-domain formulation

The compressible NS equations are a system of nonlinear partial differential equations (PDEs) expressing the conservation of mass, momentum and energy in a viscous fluid flow. Averaging the NS equations on the longest time-scales of turbulence yields the so-called RANS equations, which feature additional terms depending on the Reynolds stress tensor. Making use of Boussinesq approximation, this tensor is expressed as the product of the strain rate tensor and a turbulent or eddy viscosity. In the COSA CFD code, the latter variable is computed by means of the two-equation $k - \omega$ SST turbulence model. Thus, turbulent flows are determined by solving a system of $N_{pde} = 6$ PDEs in two dimensions and $N_{pde} = 7$ in three dimensions.

Given a moving control volume $\mathcal{C}$ with time-dependent boundary $S(t)$, the Arbitrary Lagrangian-Eulerian integral form of the system of the time-dependent RANS and SST equations is:

$$\frac{\partial}{\partial t}\left(\int_{\mathcal{C}(t)} \mathbf{U}\, d\mathcal{C}\right) + \oint_{S(t)} (\underline{\mathbf{\Phi}}_c - \underline{\mathbf{\Phi}}_d) \cdot d\underline{S} - \int_{\mathcal{C}(t)} \mathbf{S}\, d\mathcal{C} = 0 \tag{1}$$

where $\mathbf{U} = [\rho \quad \rho\underline{v}' \quad \rho E \quad \rho k \quad \rho\omega]'$ is the array of conservative variables, ρ, $\underline{v}$, E, k and ω are, respectively, the flow density, the flow velocity vector, the total energy per unit mass, the turbulent kinetic energy per unit mass and the specific dissipation rate of turbulent energy, and the superscript $'$ denotes the transpose operator. The total energy is $E = e + (\underline{v} \cdot \underline{v})/2 + k$, where e denotes the internal energy per unit mass; the perfect gas law is used to express the static pressure p as a function of ρ, E, k and the mean flow kinetic energy per unit mass $(\underline{v} \cdot \underline{v})/2$. The expressions of the generalized convective flux vector $\underline{\mathbf{\Phi}}_c$ and the generalized diffusive flux vector $\underline{\mathbf{\Phi}}_d$ are reported in [11].

The turbulent viscosity μ_T, required to calculate the Reynolds stress tensor [11], is given by

$$\mu_T = a_1 \rho k / \max(a_1 \omega, F_2 |\Omega_f|) \tag{2}$$

in which $a_1 = 0.31$, Ω_f is the flow vorticity, and F_2 is a function of k, ω, the molecular kinematic viscosity ν and the distance from the wall d. The expression of F_2 can be found in [30].

The definition of the source term $\mathbf{S}$ in Eqn. (1) is $\mathbf{S} = [0 \quad \underline{0}' \quad 0 \quad S_k \quad S_\omega]'$ where

$$S_k = \mu_T P_d - \frac{2}{3}(\nabla \cdot \underline{v})\rho k - D_k \tag{3}$$

$$S_\omega = \gamma \rho P_d - \frac{2}{3}(\nabla \cdot \underline{v})\frac{\gamma \rho k}{\nu_T} - D_\omega + CD_\omega \tag{4}$$

and

$$P_d = 2\left[\underline{\underline{s}} - \tfrac{1}{3}\nabla \cdot \underline{v}\right] \nabla \underline{v} \tag{5}$$

$$D_k = \beta^* \rho k \omega \qquad D_\omega = \beta \rho \omega^2 \tag{6}$$

$$CD_\omega = 2(1 - F_1)\rho \sigma_{\omega 2} \tfrac{1}{\omega} \nabla k \cdot \nabla \omega \tag{7}$$

Here ν_T is the turbulent kinematic viscosity, and the variables σ_k, σ_ω, γ, β^* and β are weighted averages of the constants of the standard $k-\omega$ model [32] and the constants of the standard $k-\epsilon$ model [33] with weights F_1 and $(1-F_1)$, respectively. The function F_1 depends on the local values of k, ω, ν, ρ, d, ∇k and $\nabla\omega$ [30], $\sigma_{\omega 2}$ is a constant of the standard $k-\epsilon$ model, and the symbol $\underline{\underline{s}}$ denotes the strain rate tensor, defined as $\underline{\underline{s}} = (\nabla\underline{v} + \nabla\underline{v}')/2$.

It can be shown that the production term P_d is always positive. Thus the source term S_k of the k-equation has a term which is always positive (production term proportional to P_d), a term which is always negative (destruction term D_k) and a term which is positive or negative depending on the sign of $\nabla\cdot\underline{v}$. Similarly to S_k, the source term S_ω of the ω-equation also has a term which is always positive (production term proportional to P_d), a term which is always negative (destruction term D_ω), and a term which is positive or negative depending on the sign of $\nabla\cdot\underline{v}$. The source term S_ω, however, features an additional cross-diffusion term CD_ω which can be positive or negative. As seen below, the identification of positive and negative source terms is of crucial importance when using a point-implicit integration of the equations of turbulence [34, 35],

2.2. Harmonic balance formulation

The derivation of the *high-dimensional* HB formulation [36] of the RANS and SST equations follows the same steps of that of the high-dimensional HB NS equations [26], and yields:

$$\Omega D\left(\int_{\mathcal{C}_H}\mathbf{U}_H\,d\mathcal{C}_H\right) + \oint_{S_H}(\underline{\mathbf{\Phi}}_{cH} - \underline{\mathbf{\Phi}}_{dH})\cdot d\underline{S}_H - \int_{\mathcal{C}_H}\mathbf{S}_H\,d\mathcal{C}_H = 0 \qquad (8)$$

where Ω is the known excitation frequency, D is the $(N_{eqs}\times N_{eqs})$ antisymmetric matrix with $N_{eqs} = [N_{pde}\times(2N_H+1)]$ defined in [26], and N_H is the user-given number of complex harmonics retained in the truncated Fourier series approximating the sought periodic flow field, The unknown array $\mathbf{U}_H$ is made up of $2N_H+1$ flow states or snapshots, referring to the equally spaced points of one period:

$$t_n = \frac{n}{(2N_H+1)}\frac{2\pi}{\Omega}, \qquad n = 0, 1, \ldots, 2N_H \qquad (9)$$

and its definition is therefore $\mathbf{U}_H = [\mathbf{U}(t_0)' \, \mathbf{U}(t_1)' \ldots \mathbf{U}(t_{N_H})']'$. The structure of $\underline{\boldsymbol{\Phi}}_{cH}$, $\underline{\boldsymbol{\Phi}}_{dH}$, $\mathbf{S}_H$, $\mathcal{C}_H$ and $d\underline{\mathbf{S}}_H$ is similar to that of $\mathbf{U}_H$.

The high-dimensional HB method represents the frequency-domain governing equations in the time-domain, where they take the form of a set of coupled steady problems. Passing from the conventional time-domain framework to the harmonic balance framework, the number of PDEs increases from N_{pde} to $[N_{pde} \times (2N_H + 1)]$. Despite this, however, the HB approach allows turbulent periodic flows to be computed at a significantly lower computational cost than with the TD approach in many problems of engineering interest.

3. Numerical method

3.1. Space discretization

The finite volume cell-centered parallel CFD code COSA [37, 26, 38, 39] solves the integral form of both the TD conservation laws (System (1)) and the HB conservation laws (System (8)) using structured multi-block grids. In moving-body problems, the governing equations are solved in the absolute frame of reference, where the whole computational grid moves with a rigid body motion conforming to the user-given motion of the considered geometry (*e.g.* rotor blade).

The discretization of the convective fluxes of both RANS and SST PDEs is based on Van Leer's second order $MUSCL$ extrapolations and Roe's flux-difference splitting. Van Albada's flux limiter has been used for all simulations reported in this paper. The discretization of the diffusive fluxes and the turbulent source terms is based on second order finite-differencing, as reported in [37]. That article also provides the definitions of the viscous wall and far field boundary conditions used by COSA.

For steady problems the time-derivative appearing in System (1) vanishes and, for each cell of a computational grid, the discretized form of that system of PDEs becomes a system of N_{pde} nonlinear algebraic equations of the form:

$$\mathbf{R}_\Phi(\mathbf{Q}) = 0 \tag{10}$$

The N_{pde} entries of $\mathbf{Q}$ are the unknown conservative variables at the cell center, whereas the N_{pde} entries of $\mathbf{R}_\Phi$ store the cell residuals.

3.2. Integration of steady equations

The RANS and SST equations are solved with a pseudo-time-marching algorithm using the so-called fully coupled approach [34, 35] whereby the two sets of equations are time-marched simultaneously. The unknown flow vector $\mathbf{Q}$ is computed by solving iteratively Eqn. (10). A fictitious time-derivative ($d\mathbf{Q}/d\tau$) premultiplied by the cell volumes is added to this system, and this derivative is then discretized with a four-stage Runge-Kutta (RK) scheme. The numerical solution is time-marched until the steady state is achieved. The convergence rate is enhanced by means of local time-stepping, variable-coefficient central implicit residual smoothing (IRS) and a full-approximation scheme multigrid (MG) algorithm. When solving turbulent problems using a two-equation turbulence model, however, this integration method becomes numerically inefficient due to the operator stiffness associated with the large negative source terms of the turbulence model. To alleviate this problem, a point-implicit integration strategy is adopted [34], whereby the abovesaid source terms are treated implicitly within each RK stage. Adopting this approach (see [37] for the detailed derivation), the steady turbulent point-implicit RK (PIRK) smoother reads:

$$
\begin{aligned}
&\mathbf{W}^0 = \mathbf{Q}_l \\
&(I + \alpha_m \Delta\tau A)\mathbf{W}^m = \mathbf{W}^0 + \alpha_m \Delta\tau A \mathbf{W}^{m-1} - \\
&\quad \alpha_m \Delta\tau V^{-1} L_{IRS}[\mathbf{R}_\Phi(\mathbf{W}^{m-1}) + \mathbf{f}_{MG}] \;, \qquad m = 1,4 \\
&\mathbf{Q}_{l+1} = \mathbf{W}^M
\end{aligned}
\tag{11}
$$

where $\Delta\tau$ is the local pseudo-time-step, V is the cell volume, l is the RK cycle counter, m is the RK stage index, α_m is the m^{th} RK coefficient, L_{IRS} denotes the IRS operator, and $\mathbf{f}_{MG}$ is the MG forcing function. The only nonzero elements of the $(N_{pde} \times N_{pde})$-matrix A are the elements of an upper triangular matrix making up its bottom right (2×2) partition, given by:

$$
A(5:6,5:6) = \begin{bmatrix} (\Delta^+ + \beta^* \omega) & \beta^* k \\ 0 & \gamma \Delta^+ + 2\beta\omega \end{bmatrix}
\tag{12}
$$

in which $\Delta^+ = \max(0, \frac{2}{3}\nabla \cdot \underline{v})$. Eqn. (12) is the exact term resulting from the point-implicit integration of the $k-\omega$ model, but it is instead an approximation in the case of the SST model. The exact term for the SST case has also a nonzero (5,6) entry [37]. Numerical experiments, however, reveal that the results computed with either Eqn. (12) or the exact matrix partition $A(5:6, 5:6)$ of the SST model differ by negligible amounts. The use of Eqn. (12) also enables to update ρk and $\rho\omega$ using successive substitutions and avoiding more costly matrix inversions. For these reasons, COSA uses Eqn. (12) also for the SST model.

In order to prevent the specific dissipation rate $\rho\omega$ from taking unphysically low values, the value of this variable obtained with Algorithm 11 is limited by the minimum threshold:

$$(\rho\omega)_{min} = \gamma\rho\sqrt{P_d} \tag{13}$$

as suggested in [34]. In the authors' experience, the use of Eqn. (13) yields substantial improvements of the numerical stability of the presented integration approach for most turbulent problems considered thus far, including those reported in this article. It is also noted that the partial decoupling of the update process of the two turbulent variables enabled by the upper triangular form of $A(5:6, 5:6)$ allows a straightforward application of the constraint expressed by Eqn. (13): one first updates $\rho\omega$ with the sixth component of one PIRK stage, then constrains the new value of $\rho\omega$ with Eqn. (13), and finally updates ρk with the fifth component of the same PIRK stage making use of the constrained $\rho\omega$. Thus far, the authors' experiments aimed at incorporating Eqn. (13) in the exact formulation of the SST variables update, which features a nonzero $A(6, 5)$, have resulted in a dramatic reduction of the numerical stability of the fully coupled integration of the RANS and SST equations. Such stability reduction is even stronger for time-domain and harmonic balance problems, and for this reason COSA uses Eqn. (12) also for these simulations.

In the present implementation of the SST turbulence model, the production terms of both k and ω are limited with an approach similar to that proposed by Menter in [40]. This is accomplished by applying the following limiter to the production term P_d appearing in Eqns. (3 and (4):

$$\tilde{P}_d = \min\left(P_d, \frac{l_k D_k}{\mu_t}\right) \tag{14}$$

where $\tilde{P}_d$ is the limited production term used to build the residuals of k and ω, and l_k is a user-given constant. The article [40] proposes $l_k = 20$, and reports that this limiter has two functions, namely to: a) 'eliminate the occurrence of spikes in the eddy viscosity due to numerical "wiggles" in the strain rate tensor $\underline{\underline{s}}$', and b) 'eliminate the unphysical build-up of eddy viscosity in the stagnation region of an airfoil'. For relatively simple problems, the solutions obtained with and without the use of Eqn. (14) differ very little. However, in the case of complex unsteady flows, such as those associated with VAWT rotors, the solutions obtained with and without the limiter of Eqn. (14) may differ significantly, as observed in section 5.

The integration of the TD RANS and SST equations is accomplished by using the same strongly coupled point-implicit approach reported above within a dual-time-stepping algorithm with second order accuracy in the physical time. The point-implicit treatment of the unknown source term arising from the time-discretization of the physical time-derivative of both RANS and SST equations is also adopted [41] (the algorithmic details are provided in [37]. The resulting TD PIRK smoother enables the use of higher Courant Friedrichs Lewis (CFL) numbers than the conventional TD fully explicit RK (FERK) smoother [37, 38]. The TD PIRK approach does not require any additional costly operation with respect to the TD FERK approach. Thus, the TD PIRK method reduces the simulation runtime proportionally to the reduction of the the MG cycles required to achieve a prescribed reduction of the residuals.

Since the PIRK treatment of the negative source terms of the SST model is used by all COSA solvers, in the remainder of this report the acronyms PIRK and FERK will be used only with reference to the numerical treatment of the unknown source term arising from the discretization of the time-derivative in the TD equations, and the source term associated with the HB counterpart of the time-derivative of the TD equations (this term is introduced in next subsection).

3.3. Integration of harmonic balance equations

The only difference between Systems (1) and (8) is that the physical time-derivative of the former system is replaced by a volumetric source term proportional to Ω in the latter. The set of nonlinear algebraic equations resulting from the space discretization of System (8) is thus solved with the same technique used for steady problems. The HB solution $\mathbf{Q}_H$ at each cell center is obtained by solving the system of algebraic equations:

$$\mathbf{R}_{gH}(\mathbf{Q}_H) = \Omega V_H D\mathbf{Q}_H + \mathbf{R}_{\Phi H}(\mathbf{Q}_H) = 0 \tag{15}$$

The array $\mathbf{Q}_H$ is made up of $(2N_H+1)$ flow states, each referring to the physical times defined by Eqn. (9), and has length $[N_{pde} \times (2N_H+1)]$. The first N_{pde} elements of $\mathbf{Q}_H$ contain the flow state at $t = t_0$, the next N_{pde} elements contain the flow state at $t = t_1$, and so on. The arrays $\mathbf{R}_{gH}$ and $\mathbf{R}_{\Phi H}$ have the same structure of $\mathbf{Q}_H$. The $(2N_H+1)$ states of $\mathbf{R}_\Phi$ contain the residuals associated with the convective fluxes, the diffusive fluxes and the turbulent source terms at the considered physical times. The residual array $\mathbf{R}_g$ also includes the source term $\Omega V_H D\mathbf{Q}_H$, where V_H is an array containing the values of the cell volume at the considered times.

The HB-counterpart of the turbulent steady smoother (11) is:

$$\begin{aligned}
&\mathbf{W}_H^0 = (\mathbf{Q}_H)_l \\
&[I + \alpha_m \Delta\tau_H A_H]\,\mathbf{W}_H^m = \mathbf{W}_H^0 + \alpha_m \Delta\tau_H A_H \mathbf{W}_H^{m-1} - \\
&\quad \alpha_m \Delta\tau_H V_H^{-1} L_{IRS,H}[\mathbf{R}_{gH}(\mathbf{W}_H^{m-1}) + \mathbf{f}_{MG,H}]\,, \qquad m = 1,4 \\
&(\mathbf{Q}_H)_{l+1} = \mathbf{W}_H^M
\end{aligned} \tag{16}$$

where the array $\Delta\tau_H$ has $(2N_H+1)$ entries containing the local time-steps for the $2N_H+1$ flow states. The HB MG forcing term $\mathbf{f}_{MG,H}$ has the same structure of $\mathbf{Q}_H$. The block-diagonal matrix A_H has $2N_H+1$ blocks of dimension $[N_{pde} \times N_{pde}]$, each referring to one of the $2N_H+1$ states. The structure of each block is the same as that of the matrix A in Algorithm (11). The HB IRS operator $L_{IRS,H}$ has the same block structure of A_H.

When using Eqn. (12) for the update of ρk and $\rho\omega$, the structure of the matrix premultiplying $\mathbf{W}_H^m$ at the second line of Algorithm (16) is such that, for each grid cell, the update of the $[N_{pde} \times (2N_H+1)]$ unknowns does not require any matrix inversion. It is also noted that Algorithm (16) uses a FERK treatment of the HB source term $\Omega V_H D \mathbf{Q}_H$. In the light of the superior convergence rate of the PIRK over the FERK integration for turbulent TD flows solved with the RANS and SST equations [37], it is expected that a point-implicit treatment of the HB source term [11] may enable the use of larger CFL numbers, thus further increasing the convergence rate of the HB equations. The HB PIRK integration, however, increases the computational cost of each RK stage, because, for each cell, it requires the inversion of two matrices of size $[(2N_H + 1) \times (2N_H + 1)]$ for updating k and ω. The convenience of the approach depends on whether the faster convergence enabled by higher CFL numbers outweighs the additional burden of the matrix inversions. This feature is case-dependent, and for all simulations reported in this article, the HB PIRK integration did not enable the use of CFL numbers higher than those used by the HB FERK approach of Algorithm (16).

It is also noted that the ratio of the computational cost of one HB FERK MG cycle and that of one steady MG cycle grows in a slightly superlinear fashion with N_H, due to construction of the HB source term $V_H D_H \mathbf{Q}_H$. This overhead, however, remains relatively small even for very high values of N_H up to 16, as highlighted in the numerical tests provided below.

4. Horizontal axis wind turbine blade section

All COSA solvers have been thoroughly verified and validated as reported in [11, 37, 26, 38, 42]. This section presents the analysis of the two-dimensional (2D) turbulent periodic flow past the airfoil of a rotating HAWT blade in yawed wind. The rotor radius is 82.0 m and the rotor speed is 12.0 RPM, which corresponds to a value of Ω of about 1.26 rad/s. The freestream wind velocity V_∞ is 13 m/s, and a yaw angle δ of 45^o is assumed. The considered section is at a distance R of 24.6 m (30 % rotor radius) from the rotational axis, and it has a chord c of 5.2 m and a twist γ_p of 10.44^o. The 2D analysis set-up is obtained using the yawed wind reduction model reported in [11], to which the reader is referred for further detail. Making use of that model, the yawed wind condition perceived by the airfoil at rotor radius R can be approximated by the unsteady 2D flow field resulting from a horizontal harmonic motion of the airfoil in a steady freestream at speed W_∞ and direction α_∞, respectively given by:

$$W_\infty = \sqrt{(V_\infty \cos\delta)^2 + (\Omega R)^2} \tag{17}$$

$$\alpha_\infty = \arctan\left[(V_\infty \cos\delta)/(\Omega R)\right] \tag{18}$$

Using these equations, one finds $W_\infty = 32.2\ m/s$ and $\alpha_\infty = 16.56^o$. Choosing the standard temperature of 288 K, the Mach number M_∞ corresponding to W_∞ and adopted in the 2D simulations is 0.095. In the 2D model, the mesh is built past the twisted airfoil, and the angle ϕ_∞ between the freestream at speed W_∞ and the chord (angle of attack) is thus $\phi_\infty = \alpha_\infty - \gamma_p = 6.12^o$. The expression of the harmonic motion is:

$$h(t) = h_0 \sin(\Omega t) \tag{19}$$

$$h_0 = V_\infty \sin\delta/\Omega \tag{20}$$

Each period of the 2D harmonic motion corresponds to a revolution of the turbine rotor. Inserting the data provided above into Eqn. (20) gives $h_0 = 1.4c$. The reduced frequency is $\lambda = \Omega c/W_\infty = 0.203$.

The blade section features the *DU99 W 350LM* airfoil, which has a maximum thickness-to-chord ratio of 35 percent. The Reynolds number based on the standard density of 1.22 kg/m^3, the velocity W_∞, the airfoil chord and the air viscosity at standard temperature is 1.15×10^7. The $524,288$-cell C-grid adopted for all simulations has 512 mesh intervals along the airfoil, 256 intervals in the grid cut, and 512 intervals in the normal-like direction. The far field boundary is at about 50 chords from the airfoil, and the distance d_w of the first grid points

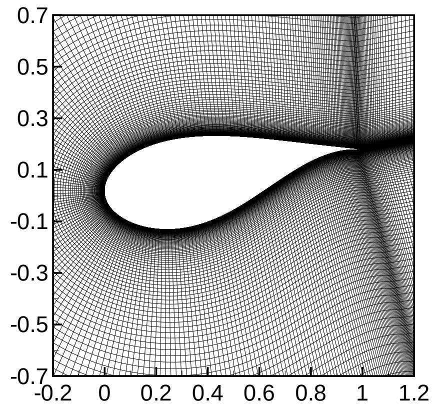

Figure 1: HAWT blade section test case: grid view in airfoil region (only every second line in both directions is plotted).

off the airfoil surface from the surface itself is about $10^{-6}c$. The nondimensional minimum distance from the wall is $y^+ = (u_\tau d_w)/\nu_w$, where u_τ is the friction velocity and ν_w is the kinematic viscosity at the wall. In all the simulations reported below, the maximum value of y^+ was always smaller than 1.

As mentioned above, the airfoil and the whole grid are inclined by the twist angle γ_p on the horizontal direction, and Fig. 1 provides an enlarged view of the adopted grid in the airfoil region. For visual clarity, only every second line of both grid line sets is plotted. In the unsteady simulations, the whole grid undergoes a sinusoidal motion defined by Eqn. (19), with amplitude h_0 given by Eqn. (20). All steady, TD and HB simulations have been performed using the MG solver with 3 grid levels. No CFL ramping has been used, and the CFL number has been set to 4 from the beginning of all simulations.

4.1. Aerodynamic analyses

To determine the minimal time-resolution of the TD analysis required to obtain a solution independent of further reductions of the physical time-step, four different TD simulations have been performed using a number of physical time-steps per period N_p of 256, 128, 64, and 32. In the discussion below, these simulations are denoted by $TD \quad N_p$. Three force coefficients have been monitored in the simulations: the horizontal force coefficient C_x, the vertical force coefficient C_y, and the constant-head pitching moment coefficient C'_m, defined respectively as:

$$C_x = \frac{F_x}{0.5\rho_\infty W_\infty^2 c} \qquad C_y = \frac{F_y}{0.5\rho_\infty W_\infty^2 c} \qquad C'_m = \frac{M}{0.5\rho_\infty W_\infty^2 c^2}$$

The horizontal force per unit blade length F_x is the tangential force component that results in useful torque; the vertical force per unit blade length F_y is the axial force component that results in rotor thrust; the pitching moment per unit blade length M at one quarter chord from the leading edge provides a measure of the torsional aerodynamic load on the blade. All four TD simulations have been run until the maximum C_x, C_y and C'_m differences over two consecutive oscillation cycles became less than 0.1 % of their maxima over the latter cycle of the cycle pair.

The coefficients C_x, C_y and C'_m are all constant-head force coefficients. A variable-head force coefficient set is also considered below, namely the standard lift force coefficient C_l, the drag coefficient C_d, and the quarter-chord pitching moment coefficient C_m. The force coefficients C_l and C_d differ from C_x and C_y not only because they consider different force components, but also because the dynamic head at the denominator of C_l and C_d is that associated with the relative time-dependent freestream velocity $\underline{W}_\infty^r$, which has components

$$W_x = \Omega R - V_\infty \sin(\delta)\cos(\Omega t)\ , \qquad W_y = V_\infty \cos(\delta) \tag{21}$$

and forms an angle α_∞^r with the horizontal direction given by:

$$\alpha_\infty^r = \arctan(W_y/W_x) \tag{22}$$

The coefficients C_m and C'_m also differ because of the different definition of the dynamic head. It should also be noted that the directions of lift and drag change throughout the period, due to the time-dependence of α_∞^r, whereas the directions of F_x and F_y are constant. More detail on this aspect can be found in [11].

The C_l, C_d and C_m profiles over one revolution computed by the four TD analyses are depicted in the three subplots of Fig. 2. The variable along the x-axis is the percentage time of a period T. These results show that at least 64 intervals per period are required to achieve lift and drag predictions independent of further increments of the time resolution, whereas at least 128 intervals per period are required for a temporal grid-independent estimate of the pitching moment. The TD 128 simulation is therefore taken as the reference TD result. The three subplots of Fig. 2 also report the profile of the angle ϕ^r_∞ between the time-dependent freestream velocity $\underline{W}^r_\infty$ defined by Eqn. (21) and the chord over the period. One has $\phi^r_\infty = \alpha^r_\infty - \gamma_p$, with α^r_∞ defined by Eqn. (22). The angle ϕ^r_∞ can be taken as an estimate of the time-dependent angle of attack (AoA). It is observed that ϕ^r_∞ is maximum at the beginning of the period ($h(0) = 0$), when the blade is at the vertical position where the blade velocity and the yawed wind velocity component have opposite direction, and is minimum at the period midpoint ($h(0.5T) = 0$), where the blade is at the vertical position where the blade velocity and the yawed wind velocity component have the same direction. All three subplots of Fig. 2 highlight that the force cycles are significantly hysteretic, and this is due to the occurrence of dynamic stall. To emphasize this feature, four positions are considered and labeled 1 to 4 in the first two subplots. They denote respectively the 5, 30, 70 and 95 percent positions of the period. The symbol Δ_l in the top left subplot indicates the C_l difference between positions 1 and 4, which both have the same value of ϕ^r_∞. Such difference occurs because towards 95 percent of the period the blade section starts stalling, and the lift recovery in the descending branch of ϕ^r_∞ lags the lift increment in the ascending branch, as often observed in the presence of dynamic stall. The symbol Δ_d in the top right subplot indicates the C_d difference between positions 2 and 3, which both have the same value of ϕ^r_∞. As discussed below, such difference occurs because the viscous wall stress on the rear portion of the airfoil pressure side at 30 percent of the period is higher than at 70 percent of the period. It should be noted that, since the dynamic head and the relative flow direction used to compute the C_l, C_d and C_m coefficients vary during the period, these coefficients do not provide a direct measure of the section contribution to the aerodynamic loads acting on the blade. Direct measures of the forces acting on the blade section are instead provided by the constant-head coefficients C_x, C_y and C'_m examined later in this subsection.

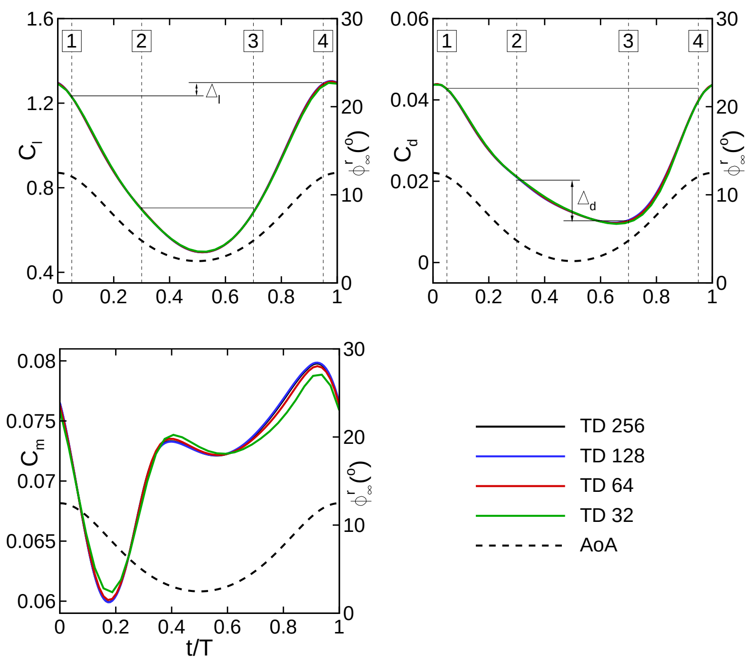

Figure 2: HAWT blade section test case: periodic profiles of variable head force coefficients over one period computed with four TD analyses. Top left: lift coefficient; top right: drag coefficient; bottom left: pitching moment coefficient.

The four subplots of Fig. 3 show the $TD\,128$ contours of flow vorticity Ω_f and the streamlines past the blade section at the positions labeled 1 to 4 in Fig. 2. The top left and bottom right subplots refer respectively to the positions at 5 and 95 percent of the period, and their comparison confirms that the amount of flow reversal in the rear portion of the airfoil suction side is larger at 5 percent of the period, which is the main reason why the lift in this position is lower than that at 95 percent of the period. The top right and bottom left subplots refer instead to the positions at 30 and 70 percent of the period respectively. Their

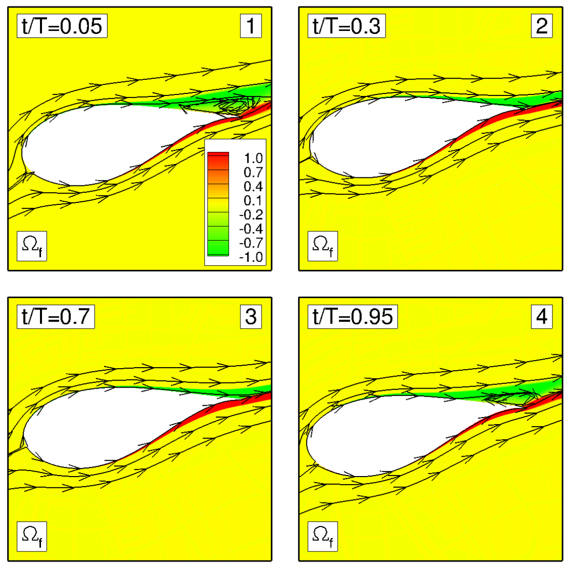

Figure 3: HAWT blade section test case: snapshots of vorticity contours and streamlines at four positions labeled 1 to 4 in Fig. 2 computed with TD 128 simulation. Top left: 5 % of the period; top right: 30 of the % period; bottom left: 70 % of the period; bottom right: 95 % of the period.

comparison reveals that in the former position the amount of vorticity on the rear portion of the airfoil pressure side is smaller than in the latter position. This is due to higher velocity of the air stream when the airfoil is at 30 percent of the period, and it results in a thinner boundary layer and a consequently higher viscous stress at the wall. This is the main reason for the higher drag in most of the first half of the period.

To provide further insight into the main characteristics of the hysteretic phenomena discussed above, the static pressure coefficient c_p and the skin friction coefficient c_f at the four selected positions of the period are examined in Fig. 4. The definitions of c_p and c_f are respectively:

$$c_p = \frac{p_w - p_\infty}{0.5\rho_\infty (W^r_\infty)^2} \tag{23}$$

$$c_f = \frac{|\tau_w|}{0.5\rho_\infty (W^r_\infty)^2} \tag{24}$$

in which the symbols p_w and τ_w denote respectively the static pressure and the viscous stress at the airfoil surface. The left subplot of Fig. 4 compares the c_p profiles along the airfoil chord at 5 and 95 percent of the period. In the former position the suction side profile between 40 and 60 percent of the chord is steeper than in the latter position. As a consequence, the flat c_p region in the rear suction side region is more pronounced, which is a consequence of the higher amount of flow reversal discussed above. The right subplot of Fig. 4 compares the c_f profiles along the airfoil chord at 30 and 70 percent of the period. In the former position the pressure side profile between 60 and 90 percent of the chord is higher than in the latter position. This is a consequence of the higher air velocity in this airfoil area in the first half of the period.

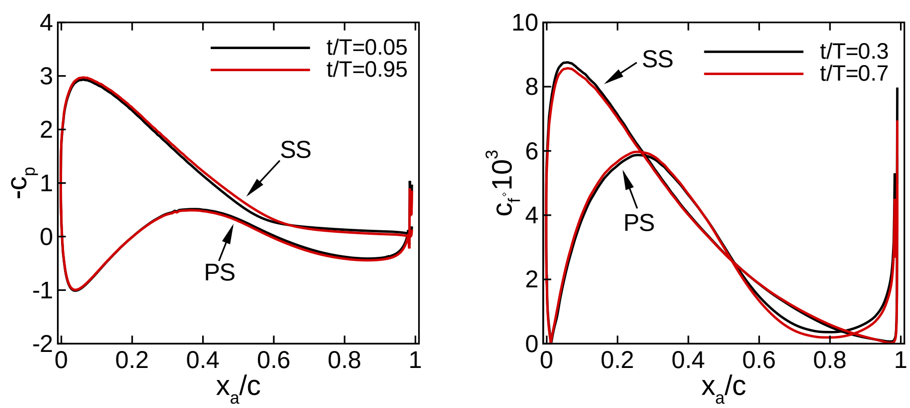

Figure 4: HAWT blade section test case. Left: static pressure coefficient at 5 and 95 percent of the period; right: skin friction coefficient at 30 and 70 percent of the period. All profiles refer to TD 128 simulation.

To determine the minimum number of harmonics required to resolve the time-dependent problem at hand with the HB solver achieving a time resolution comparable to that of the TD 128 simulation, five HB simulations have been performed. Such simulations use values of N_H of 1, 2, 3, 4 and 5, and are denoted by the acronym HB followed by the value of N_H. The hysteretic cycles of the C_x, C_y and C'_m force coefficients computed by the five HB analyses are plotted against ϕ^r_∞ in the three subplots of Fig. 5. One notes that using four complex harmonics is sufficient to achieve a resolution of the force coefficients fairly similar to that of the TD 128 simulation, as highlighted by the closeness of the TD 128 and the HB 4 solutions. It is also observed that a complete reconstruction of the flow unsteadiness by means of the HB solver requires five complex harmonics, as underlined by the fact that the TD 128 and the HB 5 hysteretic loops are superimposed.

The noticeable size of the hysteresis loops of Fig. 5 also highlights that the level of nonlinearity of the periodic flow field caused by the yawed wind condition requires the use of nonlinear CFD. The use of linear CFD is likely to yield insufficiently accurate estimates of the time-dependent loads required for reliable fatigue and aeroelastic analysis and design of HAWT blades. The C_x and C_y loops highlight a periodic variation of the contribution of this section to the rotor torque and thrust of about ± 22 % and ± 12 respectively. The variation of the C'_m coefficient with respect to its mean value is about ± 52 %, pointing to significant contributions to the blade torsional loads caused by the yawed wind regime. The angles ϕ^r_∞ and α^r_∞ take their maximum when the blade is vertical and the blade velocity and the yawed wind velocity component have opposite direction, whereas they take their minimum when the blade is vertical and the blade velocity and the yawed wind velocity component have the same direction. Therefore, Fig. 5 highlights that the maximum of all three components of the aerodynamic load occurs when the blade moves in the direction of the yawed wind component, whereas the minimum occurs when the blade moves against the yawed wind component.

It should be noted that the aerodynamic analyses reported above differ significantly from those reported in [11] for the same operating conditions. This is because that paper used the *DU91 W2 250LM* airfoil, which has a maximum thickness-to-chord ratio of 25 percent. The significantly thicker airfoil used in the present study is more representative of the inboard sections of utility-scale HAWTs, and it also results in higher levels of unsteady flow nonlinearity, a fea-

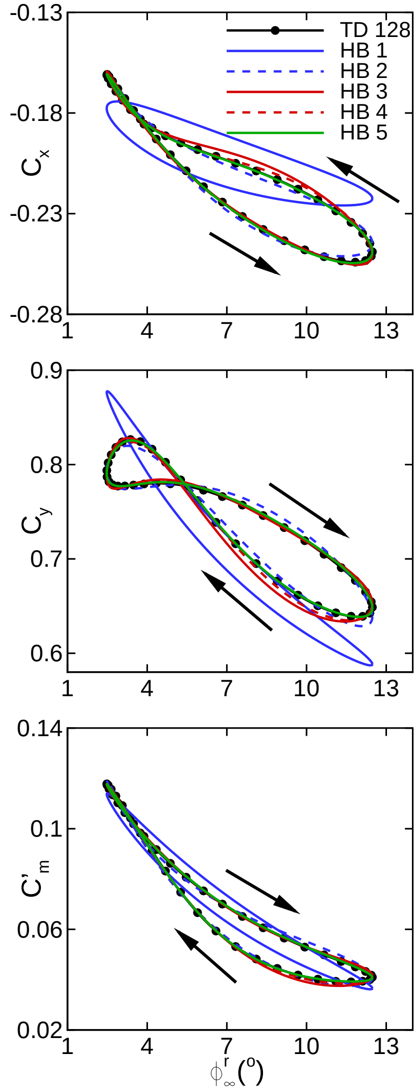

Figure 5: HAWT blade section test case: hysteretic loops of constant head force coefficients computed with five HB simulations and TD 128 simulation. Top: horizontal force coefficient; middle: vertical force coefficient; bottom: pitching moment coefficient.

ture that poses higher computational challenges to the HB RANS technology.

4.2. Computational performance of the HB solver

All HB analyses have been run for $20,000$ MG cycles, since this was the minimum value required for the convergence of all harmonics of all the force components of these five HB analyses. Each physical time-step of the TD 128 analysis has instead used $2,000$ MG iterations, as this value was that required for the convergence of all force components. In order to reduce the periodicity error below the 0.1 % threshold defined at the beginning of the previous subsection, six revolutions had to be simulated starting from a freestream initial condition. For both the HAWT blade section considered in this study and that analyzed in [11], it has been observed that the number of MG cycles required for the convergence of all harmonics of all the force components is fairly independent of N_H. The reasons why this number is $20,000$ in the present study, and $14,000$ in [11] is not only that the unsteady aerodynamics of the problem considered herein is more complex, but also that significantly different multigrid parameters were adopted in the two studies. Here all HB, TD and steady HAWT simulations used 3 smoothing cycles on the fine and medium grids, and 2 smoothing cycles on the coarse grid; all simulations of in [11] used instead 5 smoothing cycles on the fine and medium grids, and 2 smoothing cycles on the coarse grid.

The residual convergence histories of the five HB analyses over the first $8,000$ MG cycles, and the mean residual convergence history of the last period of the TD 128 simulation are reported in Fig. 6. The variable on the x-axis is the number of MG cycles. For the HB analyses, the variable Δl_r on the y-axis is the logarithm in base 10 of the normalized RMS of all cell-residuals of the four RANS equations of the $2N_H + 1$ snapshots. For the TD 128 analysis, the variable Δl_r on the y-axis is instead the logarithm in base 10 of the RMS of all cell-residuals of the four RANS equations of the 128 physical times of the last period. For both TD and HB simulations, each residual history curve is normalized by the RMS value at the first MG cycle. An interesting feature is that the convergence histories of all HB analyses are fairly close to each other. Some more noticeable differences only exist between the HB 1 curve on one hand, and the other four HB curves on the other. This occurrence points to the fact that the periodic flow nonlinearity is dominated by the first two harmonics: the contribution of the progressively smaller higher-frequency harmonics of the $HB\,3$, $HB\,4$ and $HB\,5$ analyses does not affect significantly the spectrum of the linearized operator associated with the integration of these HB set-ups with respect to that associated with the HB 2 set-up. The dominance of the first two harmonics in the Fourier reconstruction of this periodic flow is also confirmed by the HB hysteretic force loops of the subplots of Fig. 5. Inspection of these curves reveals that the largest differences among the HB results are those between the HB 1 simulation on one hand and the other four HB simulations on the other. This highlights a significant contribution of the second harmonic to the periodic flow, and rapidly decreasing contributions of the higher order harmonics. Figure 6 also reports the convergence history of the steady problem obtained from the HB set-up by only turning-off the grid motion. The curve of the steady residual history does not differ substantially from those of the HB analyses, and this provides further indication that the level of flow unsteadiness in the problem at hand is moderate.

When using the HB FERK MG smoother given by Eqn. (16) to solve the HB RANS and SST equations, the CPU-time of one HB MG iteration increases in a moderately superlinear fashion with N_H. This implies that, for a given number of computer cores used for the simulation, the runtime of a HB N_H simulation with a given number of MG cycles is higher than $(2N_H + 1)$ times the runtime of the steady simulation using the same number of MG cycles. This overhead is due to the calculation of the HB source term $\Omega V_H D\mathbf{Q}_H$ appearing in Eqn. (15), and is proportional to $(2N_H+1)^2$. Such an overhead can be quantified by taking the ratio of the measured CPU-time of one MG iteration of the HB N_H analysis and that of one MG cycle of the steady analysis, and dividing such a ratio by $(2N_H + 1)$. The variable C_{MG} thus obtained is reported in the second row of Table 1. It is seen that the overhead for the calculation of the HB source term with the HB 5 analysis makes the average CPU-time of one HB MG cycle about 7 percent higher than that of one steady MG cycle.

The HB *speed-up* parameter, defined as the ratio of the runtime of the

TD 128 simulation and the HB analysis for the five values of N_H, is reported in the third row of Table 1. It is seen that the HB 4 simulation, which yields a very good estimate of the time-dependent loads, reduces the analysis runtime by a factor 8 with respect to the fully time-resolved TD 128 analysis. The HB 5 analysis, yielding the same resolution of the TD 128 analysis reduces the analysis runtime by a factor 6.5, which is still a remarkable benefit for practical applications.

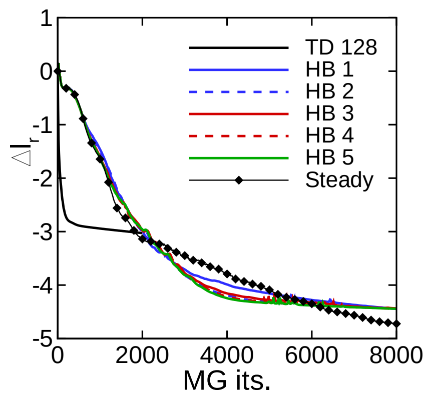

Figure 6: HAWT blade section test case: residual convergence histories of steady, TD and HB solvers.

Table 1: HAWT blade section test case: overhead parameter C_{MG} of HB MG cycle with respect to steady MG cycle, and speed-up of HB analyses with respect to TD 128 analysis.

	HB 1	HB 2	HB 3	HB 4	HB 5	TD 128	steady
C_{MG}	1.038	1.044	1.056	1.066	1.073	—	1.00
speed-up	24.7	14.7	10.4	8.0	6.5	1.0	—

5. H-Darrieus rotor section

Here the periodic flow of a H-Darrieus wind turbine is considered. The blade airfoils of this turbine are stacked along straight lines parallel to the turbine rotational axis. Away from the blade tips, the flow can be considered two-dimensional. The considered rotor has a radius R_D of 515 mm, and its 3 blades feature the NACA0021 airfoil with a chord of 85.8 mm. The blade/spoke attachment is at 25 % chord from the airfoil leading edge. The analyzed operating condition is characterized by a freestream velocity W_∞ of 9 m/s, and a rotational speed of 550 RPM. Using standard thermodynamic conditions and the rotor circumferential speed as reference velocity, the Reynolds number based on the airfoil chord is 1.7×10^5; the Mach number associated with the circumferential speed of the rotor is 0.087. This case study was first reported and analyzed in [43] and [44], and later in several other studies, including [45].

VAWT rotor flows are inherently unsteady because the freestream conditions perceived by each blade vary periodically with frequency determined by the rotor angular speed. Starting by temporarily neglecting the fact that the absolute velocity decreases across the rotor due to the energy transfered from the fluid to the turbine, the modulus of the relative wind velocity $\underline{W^r_\infty}$ at the rotor radius R_D, and the angle ϕ^r_∞ between W^r_∞ and the time-dependent position of the airfoil chord are respectively:

$$W^r_\infty = W_\infty \sqrt{1 + 2\lambda_D \cos\theta + \lambda_D^2} \tag{25}$$

$$\phi^r_\infty = \arctan\left(\frac{\sin\theta}{\lambda_D + \cos\theta}\right) \tag{26}$$

Here $\lambda_D = \Omega R_D / W_\infty$ is the so-called tip-speed ratio, and the angle θ defines the azimuthal position of the reference blade. The reference blade has $\theta = 0$ when the directions of the absolute velocity W_∞ and the entrainment velocity ΩR_D are equal and opposite. The periodic profiles of M^r_∞, the Mach number associated with W^r_∞, and ϕ^r_∞ are reported in Fig. 7. These profiles have been computed using $\lambda_D = 3.3$, which is the tip-speed ratio corresponding to the operating conditions provided above. This value corresponds to near maximum power operation, and unless otherwise stated, all results presented below refer to this value of λ_D. Both curves of Fig. 7 are plotted with a solid line for $0 < \theta < 180^o$, the interval corresponding to the reference blade traveling in the upwind region of the rotor, and with a dashed line for $180^o < \theta < 360^o$, the interval corresponding to the reference blade traveling in the downwind region of the rotor. This distinction is highlighted because Eqns. (25) and (26) assume that the absolute velocity W_∞ is constant throughout the rotor. This is an acceptable approximation in the upwind region but is unacceptable in the downwind region. This is because the energy transfer occurring in the upwind region results in a reduction of the absolute velocity, yielding in turn a significant reduction of both W^r_∞ and ϕ^r_∞ in the downwind region. This phenomenon is important for the discussion of the rotor torque periodic profile reported below.

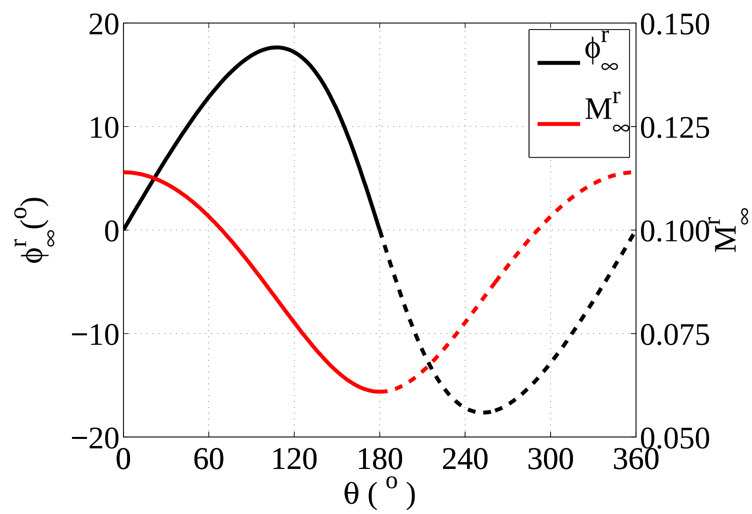

Figure 7: H-Darrieus rotor section test case: theoretical profile of relative flow angle and Mach number against azimuthal position θ of reference blade.

The physical domain containing the rotor section and its surroundings is delimited by a far field boundary centered at the rotor axis, and is discretized by a structured multi-block grid. The grid is highly clustered in the region around and between the blades, has 729,600 quadrilateral cells and is made up of two subdomains: the circular region of radius $7R_D$ containing the three blades and consisting of 522,240 cells, and the annular region with inner radius of $7R_D$ and outer radius of $240R_D$ consisting of 207,360 cells. The grid features

448 cells around each airfoil, and a distance of the first grid line off the airfoil surface from the airfoil itself of $10^{-5}c$. Enlarged views of the grid around the rotor and the airfoil leading edge areas are reported respectively in the left and right images of Fig. 8.

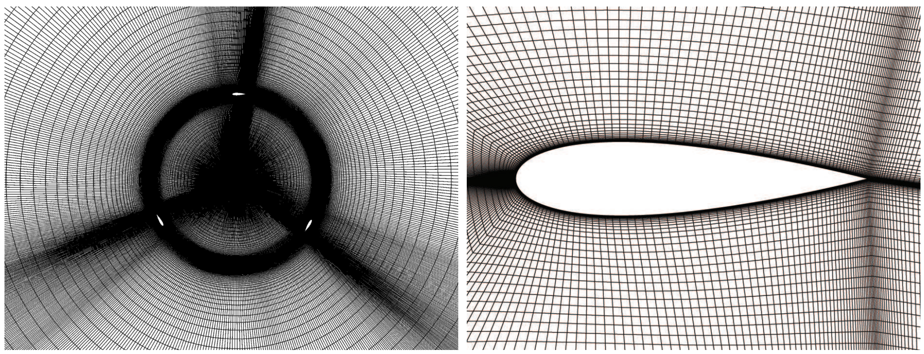

Figure 8: H-Darrieus rotor section test case. Left: grid view in rotor region; right: grid view in leading edge region. (In both cases, only every second line in both directions is plotted).

The identification of two distinct subdomains is irrelevant for the COSA analyses since the entire grid moves with the rotor. The circular interface between the two subdomains was introduced to also enable the simulation of this rotor flow with the commercial ANSYS FLUENT CFD code using the same grid of COSA. FLUENT uses a rotating and a stationary domain and requires a circular sliding interface, which was set to be the circle at distance $7R_D$ from the rotor center. The FLUENT results presented below are obtained with the coupled pressure-based solver [46]. The time-domain simulation of the same rotor flow with both codes has been performed to provide further verification evidence of the predictive capabilities of COSA. All COSA and FLUENT simulations do not use transition modeling and are fully turbulent. In all cases, the far field values of k and ω are determined by considering a turbulence intensity of 5 percent and a characteristic turbulence length of 70 mm.

All COSA TD and HB simulations discussed below have been performed using the MG solver with 3 grid levels. In all TD simulations reported below, no

CFL ramping has been used, and the CFL number has been set to 4. Conversely, CFL ramping has been used in all HB simulations, and the final CFL number has been set to 2. The fact that the maximum CFL number of the TD and HB simulations of this problem are different is not surprising. This is because the numerical operators associated with the iterative solution of the HB and TD equations are different, and feature, in general, a different spectral radius. This variable is one of the main parameters determining the maximum pseudo-time step of the iterative solution process and, thus, its highest possible CFL number and convergence rate.

5.1. Aerodynamic analyses

The grid described above is used to determine the periodic flow of the considered H-Darrieus rotor. Mesh refinement tests carried out using COSA with the grid under consideration and a finer one with twice as many grid lines in both directions, have highlighted that the present grid with 729,600 cells gives a mesh-independent solution. To determine the minimal time-resolution of the COSA TD analysis required to obtain a solution independent of further reductions of the physical time-step, four different TD simulations have been performed using a number of physical time-steps per period N_p of 1440, 720, 360, and 180. In the discussion below, these simulations are denoted by $TD\ N_p$. The starting point of each revolution is the position in which the velocity of the reference blade and the absolute velocity of the wind are parallel and opposite ($\theta = 0^o$). From here this blade describes a 180^o-circular arc trajectory traveling in the upwind region of the rotor. At the end of this phase ($\theta = 180^o$), the blade velocity and the absolute velocity of the wind are parallel and have the same orientation. Thereafter the reference blade travels back to the initial position ($\theta = 0^o$) along the 180^o-circular arc trajectory in the downwind region of the rotor.

The output variable used to monitor the convergence of the TD simulations to a periodic state is the torque coefficient C_T per unit blade length, defined as:

$$C_T = \frac{T_D}{\frac{1}{2}\rho_\infty W_\infty^2 2R_D^2}$$

where T_D is the torque acting on the reference blade. All four TD simulations have been run until the maximum C_T difference at all corresponding positions of two consecutive revolutions became less than 0.2 % of their mean value over the latter period of the cycle pair. The C_T profiles of the reference blade over one rotor revolution computed by the four TD analyses are plotted against the azimuthal position θ of the same blade in Fig. 9. These results show that at least 720 intervals per period are required to achieve a torque prediction independent of further increments of the time resolution. The TD 720 simulation is therefore taken as the reference TD result. Figure 9 also reports the C_T profile computed by FLUENT using 900 intervals per period. An excellent agreement between the prediction of the two codes is observed. The two enlarged views of Fig. 9 highlight that some very small differences between the COSA TD 720 and the FLUENT TD 900 predictions only exist around the positions $\theta = 90^o$ and $\theta = 220^o$. Several potential causes of these small differences, such as insufficient space- and/or time- resolutions of either simulation, or lack of low-speed preconditioning [47] in the simulations of the density-based COSA code, have been examined and ruled out. Possible remaining factors accounting for these small differences include a slightly different numerical implementation of the turbulence model. This type of factor, unfortunately, cannot be easily examined due to unavailability of the source code of commercial software. The COSA and FLUENT solutions, however, are extremely close, as also underlined by the fact that the mean torque predicted by the two codes differ by less than 0.15 percent. This high level of agreement constitues a new successful verification test of the COSA code for complex turbulent unsteady flow problems.

The blade torque T_D depends largely on the tangential components of the lift and drag forces acting on the blade, and both forces vary significantly during the revolution, because both the relative AoA and the modulus of the relative velocity, the flow velocity perceived by the blade, vary with θ. When the ref-

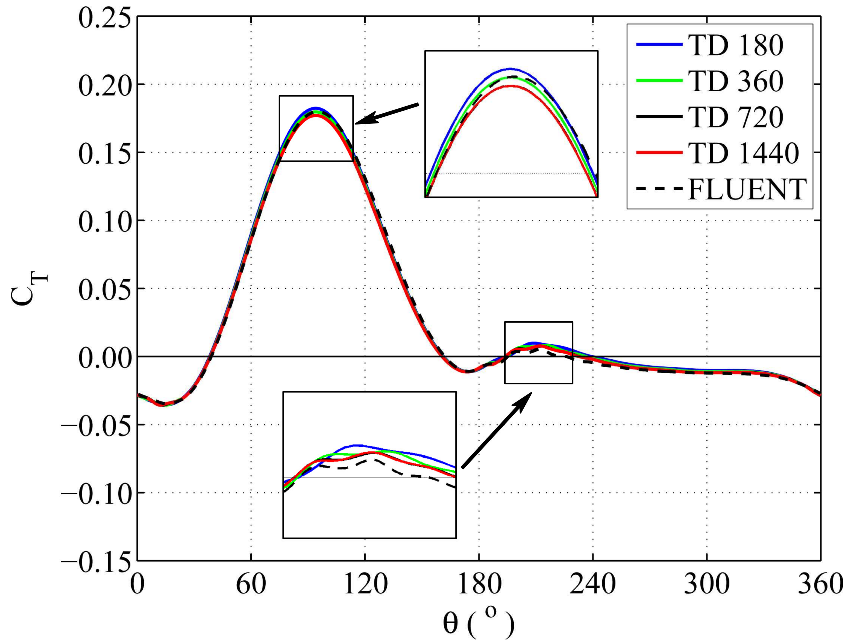

Figure 9: H-Darrieus rotor section test case: periodic profiles of torque coefficient of reference blade against azimuthal position θ computed with four COSA TD simulations, and FLUENT TD 900 simulation.

erence blade travels in the upwind region of the rotor ($0^o < \theta < 180^o$), a good qualitative estimate of the variation of the relative velocity and the AoA is provided by the M^r_∞ and ϕ^r_∞ curves of Fig. 7. This figure shows that ϕ^r_∞ achieves its maximum at $\theta \approx 90^0$. This corresponds to maximum lift coefficient of the airfoil. The peak of the torque coefficient of Fig. 9 at this azimuthal position is due to the high value of the tangential projection of the lift force. In the downwind region of the rotor, however, the absolute velocity decreases considerably with respect to its initial value W_∞, and this results in significantly lower values of the AoA in this region. This is the reason why the torque for $180^o < \theta < 360^o$ does not experience the high values and the peak observed in the first half of the period.

To discuss the main aerodynamic phenomena occurring at this operating regime, assess in further detail the differences between the COSA and FLUENT analyses, and further investigate the dependence of the COSA solution on the time step of the simulation, the blade profiles of static pressure coefficient c_p and skin friction coefficient c_f at $\theta = 0^o$, $\theta = 99^o$, and $\theta = 240^o$ are analyzed. The definitions of c_p and c_f are given respectively by Eqn. (23) and Eqn. (24). The top subplot row of Fig. 10 compares the c_p profiles of the COSA TD 360 and TD720 simulations, and the FLUENT TD900 simulation at the three azimuthal positions indicated above, whereas the c_f profiles for the same simulations and azimuthal positions are provided in the bottom subplot row. In all subplots the variable x_a/c along the x-axis is the axial position along the airfoil normalized by the chord.

The effect of the rapid increment of the AoA from its low value at $\theta = 0^o$ to its highest levels shortly before $\theta = 99^o$ is visible in the substantial loading increment between these two azimuthal positions (top left and middle subplots). Here the area between the suction side and pressure side branches of c_p is taken as a measure of the aerodynamic loading. At $\theta = 99^o$, the flow on the airfoil suction side is heavily separated due to the high AoA, as highlighted by the c_f cusp at about 50% chord (bottom middle subplot). At $\theta = 240^o$ the airfoil loading is fairly low (top right subplot) due to the reduction of the absolute velocity caused by the energy extraction from the fluid occurring in the upwind region of the rotor. The reduction of the absolute velocity results in a significant reduction of the AoA. Further detail on the analysis of this operating condition can be found in [45].

From a numerical viewpoint, one sees that the largest difference between the COSA TD360 and TD720 simulations occurs at $\theta = 99^o$, a result consistent with the differences between these two simulations observed in the torque coefficient predictions. All subplots also confirm that the overall agreement between the COSA TD 720 and and FLUENT TD 900 simulations is excellent. Fig. 10 shows that some small differences only occur in the initial part of the c_f profiles, most notably at $\theta = 99^o$ and $\theta = 240^o$. As reported above, these differences may be due to slightly different numerical implementation of the turbulence model in the two codes.

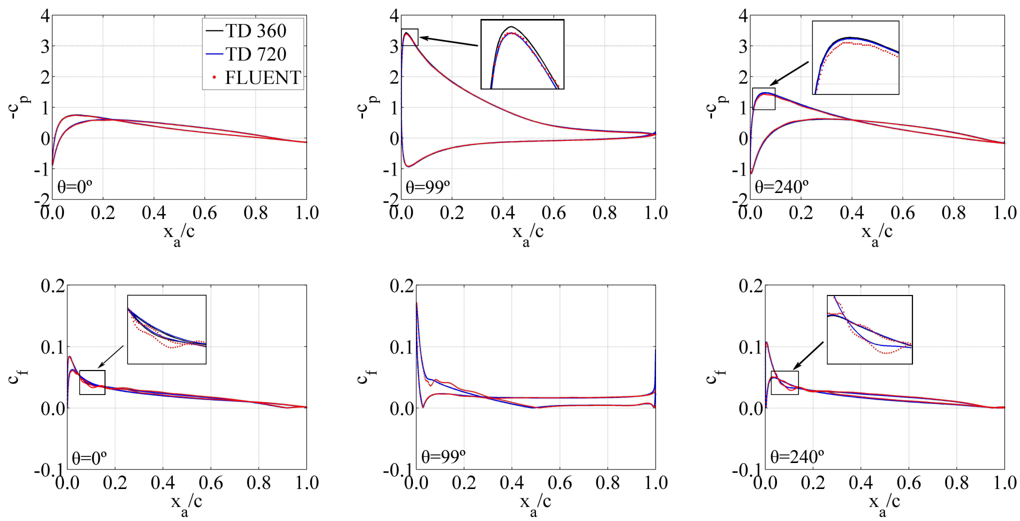

Figure 10: H-Darrieus rotor section test case: airfoil static pressure coefficient (c_p) and skin friction coefficient (c_f) of reference blade at three azimuthal positions θ computed with COSA TD 360 and TD 720 simulations, and FLUENT TD 900 simulation. Left: c_p (top) and c_f (bottom) at $\theta = 0^o$; middle: c_p (top) and c_f (bottom) at $\theta = 99^o$; right: c_p (top) and c_f (bottom) at $\theta = 240^o$.

The high level of stall associated with the highlighted flow separation at $\theta = 99^o$ is clearly visible in Fig. 11, which provides streamlines and Mach contours in the trailing edge region obtained with the COSA TD 720 simulation (left) and the FLUENT TD 900 simulation (right). Once more, an excellent agreement between the two predictions is observed.

COSA and FLUENT time-domain simulations of the H-Darrieus rotor flow considered above were also carried out in [45], but the agreement between the analyses of the two codes highlighted above is significantly better than that observed in [45]. This is because the FLUENT simulations of both studies used a limiter of the k and ω production terms similar to that of Eqn. (14) with $l_k = 10$ (this is a default setting of FLUENT), whereas no limiter of the k and ω production terms was used for the COSA simulations in [45]. On the other hand, the limiter of Eqn. (14) with $l_k = 10$ has also been used for the

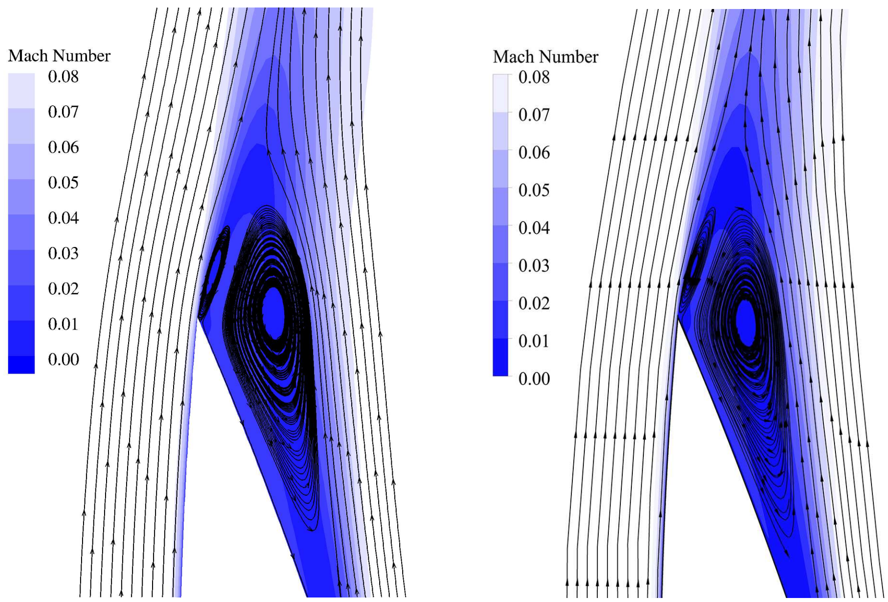

Figure 11: H-Darrieus rotor section test case: Mach contours and streamlines in reference blade trailing edge region at azimuthal position $\theta = 99^o$ computed with COSA TD 720 simulation (left) and FLUENT TD 900 simulation (right).

new COSA VAWT analyses reported herein. The significant improvement of the agreement between the predictions of the two codes emphasizes the high solution sensitivity to predominantly numerical features of complex simulation systems.

To investigate the possibility of more efficiently solving this periodic VAWT flow problem with the HB solver and assess the level of accuracy achievable by using this approach rather than the standard TD method, this $\lambda_D = 3.3$ VAWT flow field has been solved with three HB simulations. Such simulations use values of N_H of 16, 32 and 64. The periodic profiles of the torque coefficient C_T computed by these three HB analyses and the TD 720 simulation are plotted against θ in the left subplot of Fig. 12. One notes that the HB 32 and the HB 64 profiles are fairly close to each other, indicating that most of the flow periodic unsteadiness resolved by the HB analysis is contained in the first 32 Fourier modes. However, there exist some differences between these two HB

results and the reference TD 720 solution: unlike the TD profile, both of these HB profiles have some oscillations for $90^o < \theta < 180^o$, and the HB profiles also appear to slightly underpredict the torque for $180^o < \theta < 240^o$. The primary reason for these discrepancies between the TD and the HB solutions is likely to be that the residuals of the HB flow snapshots featuring the highest values of AoA, where the flow is significantly stalled, experience premature stagnation ending in a limit cycle and preventing the HB simulation from fully converging. Such premature stagnation of the residuals is a consequence of the stall induced by the high AoA. Since the high-dimensional HB method solves the frequency-domain governing equations as a set of coupled steady problems, the premature residual stagnation of the steady problems associated with the highest values of AoA ending in a limit cycle prevents the full convergence of the entire set of equations. This issue has also been reported in the dynamic stall analyses of [27]. The oscillations of the HB torque profiles for $90^o < \theta < 180^o$ reflect such limit cycles. The right subplot of Fig. 12 compares the C_T profiles of the TD 720 and the *mean* profiles of the HB 32 and HB 64 simulations. Such mean profiles are obtained by averaging the torque profiles of the last 500 MG cycles of each HB analysis. One notes that the agreement between the TD and the mean HB profiles of the torque coefficient for $90^o < \theta < 180^o$ is significantly improved, supporting the assumption that the HB 32 and HB 64 torque coefficient profiles reported in the left subplot of Fig. 12 are just instantiations of a low-level limit cycle. For this particular problem, this result is fairly independent of the number of final MG cycles of the HB simulation used to average the HB torque profile as long as this number is 300 or more. This is shown in Fig. 13, where the percentage difference of the reference blade torque averaged over the last 100, 300, 500 and 1000 MG cycles of the HB 32 simulation and the reference blade torque of the TD 720 simulation is plotted against the rotor azimuthal position θ (for each θ, the torque differences are normalized by the maximum value of the TD 720 torque profile). One sees that averaging the HB 32 torque profile over 300 MG cycles or more yields the same level of fluctuations with respect to the TD 720 estimate and maximum error amplitudes smaller than 5 percent. This averaging process is not fully consistent with the physics because the solution process of the HB equations does not correspond to a time-accurate march. However, the RK pseudo-time-marching component of the solution process is expected to qualitatively reflect unsteady flow features. For $\lambda_D = 3.3$, the averaging process yields a torque profile that differs by less than 5 percent from the reference TD estimate. This error level is likely to be acceptable for preliminary design applications. This aspect is discussed in further detail at subsection 5.3.

The interpretation of the oscillations of the HB solutions reported above is in line with the analysis of the flow physics-induced numerical instabilities of a multigrid smoother for the solution of the nonlinear NS equations and their linearized counterpart reported in [48]. It has also been found that the agreement between the TD and the HB simulations improves substantially, becoming comparable to that observed for the HAWT blade section discussed above, as the tip-speed ratio λ_D increases. This happens because the maximum AoA and the amount of flow stall decrease as λ_D increases.

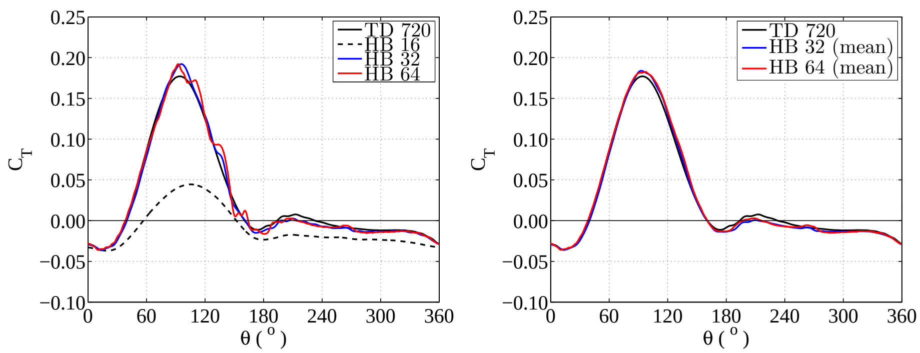

Figure 12: H-Darrieus rotor section test case: periodic profiles of torque coefficient of reference blade against azimuthal position θ computed with three COSA HB simulations, and COSA TD 720 simulation. Left: HB torque profiles at last MG cycle of simulation; right: HB torque profiles averaged over last 500 MG cycles.

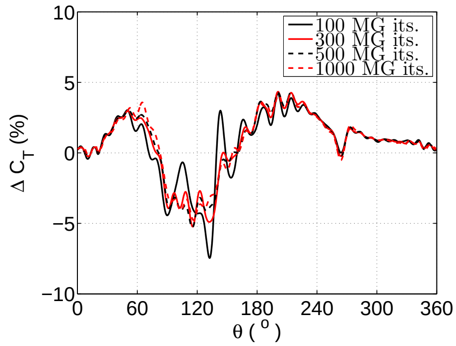

Figure 13: H-Darrieus rotor section test case: percentage difference of reference blade torque averaged over last 100, 300, 500 and 1000 MG cycles of HB 32 simulation and reference blade torque of TD 720 simulation plotted against rotor azimuthal position.

5.2. Computational performance of the HB solver

Each physical time-step of the TD 720 analysis has required 200 MG cycles to achieve a reduction of the RMS of the RANS equations of nearly seven orders. This is highlighted in the left subplot of Fig. 14, which reports the mean convergence history of the last period of the TD 720 simulation. However, it has also been verified that all force components are fully converged at all times of the revolution after just 100 cycles. In order to reduce the periodicity error below the 0.2 % threshold defined at the beginning of the previous subsection, thirty revolutions had to be simulated starting from a freestream initial condition. It has also been verified that this periodicity error threshold is achieved after thirty revolutions with both aforementioned values of the number of MG cycles per physical time.

In the case of the HB simulations, the convergence trends examined above are reversed: it has been observed that stagnation of the HB residuals is achieved long before all force components achieve a constant level. Moreover, the number of HB cycles required to achieve a constant level of all force components has been different for all three HB simulations: the HB 16, HB 32 and HB 64 have required respectively $15,000$, $12,000$ and $9,000$ MG cycles. The residual convergence histories of the three HB analyses over $12,000$ MG cycles are reported in the right subplot of Fig. 14. One notes that the mean residuals of the HB simulations decrease by only two orders before stagnating. This is most likely due to the occurrence of a limit cycle in the pseudo-time march process associated with the solution of the HB RANS and SST equations. Indeed, examination of the convergence histories of the force components associated with the 65 flow snapshots of the HB 32 simulation shows that the force components corresponding to the positions at which the AoA lies in a small neighborhood of its maximum ($90^o < \theta < 130^o$) present an oscillatory behavior about a mean value, whereas the force components corresponding to all other positions converge to fairly constant values.

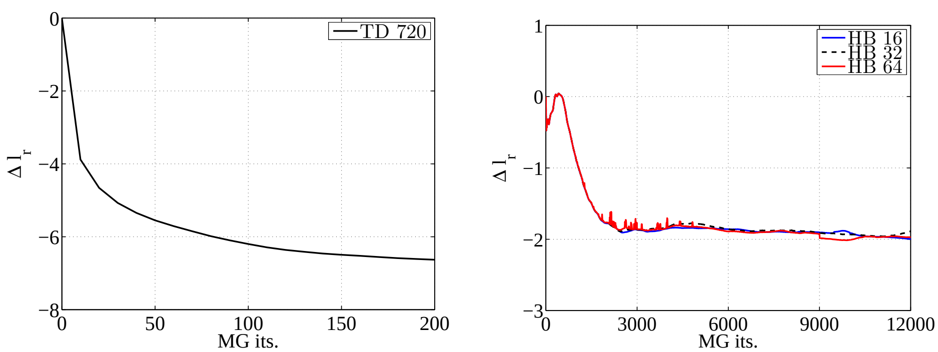

Figure 14: H-Darrieus rotor section test case: residual convergence histories of TD and HB simulations. Left: mean convergence history over last period of TD 720 simulation; right: converge histories of three HB simulations.

All TD analyses reported in this section could be performed only using the PIRK smoother [37], since the FERK integration has been found numerically stable only for unacceptably low CFL numbers. Similarly to the HAWT blade section test case, however, all HB analyses reported in this section could be performed with the FERK MG Algorithm (16). Also for the present H-Darrieus rotor section test case the overhead of the FERK HB MG cycle with respect to one steady MG cycle, arising due to the calculation of the HB source term source term $\Omega V_H D \mathbf{Q}_H$, has been analyzed. The HB overhead variable C_{MG} defined in subsection 4.2 for the three HB simulations discussed above is reported in the second row of Table 2. It is seen that the overhead for the calculation of the HB source term with the HB 32 analysis makes the average CPU-time of one HB MG cycle 50 percent higher than that of one steady MG cycle; the HB source term overhead of the HB 64 analysis makes its MG cycle more than twice as expensive as the steady MG cycle.

The HB *speed-up* parameter, defined as the ratio of the runtime of the TD 720 simulation using 100 MG cycles per physical time and the HB analysis for the three values of N_H, is reported in the third row of Table 2. It is seen that the HB 32 analysis, which brings the closest result to the TD 720 simulation is 85 percent faster than the latter analysis.

Table 2: H-Darrieus rotor section test case: overhead parameter C_{MG} of HB MG cycle with respect to steady MG cycle, and speed-up of HB analyses with respect to TD 720 analysis.

	HB 16	HB 32	HB 64	TD 720	steady
C_{MG}	1.19	1.50	2.11	—	1.0
MG cycles	15,000	12,000	9,000	2,160,000	
speed-up	3.66	1.85	0.88	1.0	—

5.3. Discussion

The HB speed-up achievable for the analysis of the H-Darrieus rotor section is significantly lower than that achieved for the analysis of the HAWT blade section. Moreover, due to the substantially higher amount of dynamic stall, the HB analysis of the VAWT problem does not enable one to achieve a solution accuracy comparable with that of the TD solution, unlike what observed for the HAWT problem.

Nevertheless, the mean power output predicted by the HB 32 analysis is in relatively good agreement with the TD 720 analysis over a wide range of tip-speed ratios. This is highlighted in Fig. 15, which shows the comparison of the rotor power curve predicted by the TD and the HB simulations for $2.4 \leq \lambda_D \leq 4$. The errors of the HB power predictions with respect to the reference TD predictions are examined in further detail in Table 3, in which the first, second, third and fourth rows report respectively the tip-speed ratio λ_D, the TD 720 power coefficient, the HB 32 power coefficient, and the percentage difference between the two power estimates. It is noted that the percentage difference between the two data sets varies between about 2 and 5 percent. The entire HB power curve could be predicted about two times more rapidly than the TD curve. As shown above, moreover, the averaged HB torque profile differs by less than 5 percent from the TD estimate. This error level is likely to be sufficiently small for structural design applications. All these occurrences bring the HB RANS CFD technology closer to the stage at which this technology may be used for preliminary VAWT rotor design, although greater runtime reductions may be required to make this technology computationally competitive with very fast low-fidelity methods, such as BEMT codes.

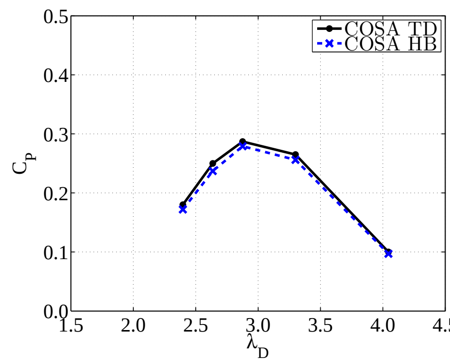

Figure 15: H-Darrieus rotor section test case: nondimensionalized power curves computed with COSA TD 720 and HB 32 simulations.

6. Conclusions

A detailed assessment of the actual benefits achievable by using a HB RANS CFD code featuring the SST turbulence model for the analysis of wind turbine periodic aerodynamics has been presented.

Table 3: H-Darrieus rotor section test case: % difference between nondimensionalized power curves computed with COSA $TD\ \ 720$ and $HB\ \ 32$ simulations.

λ_D	2.40	2.64	2.88	3.30	4.05
$C_P(TD\ \ 720)$	0.180	0.250	0.287	0.265	0.100
$C_P(HB\ \ 32)$	0.172	0.237	0.279	0.256	0.097
$\Delta C_P(\%)$	4.44	5.20	2.79	3.40	3.00

In the case of utility-scale horizontal axis machines, the assessment was based on the analysis of the periodic flow field past the 30 % blade section of a 164 m-diameter rotor in a 45^o 13 m/s yawed wind. Significant hysteresis cycles of all forces acting on the blade section were observed, with variations of the axial and tangential force components of about ± 12 % and ± 22 %, respectively, of their mean values, and variations of the sectional torque of about 52 % of its mean value. The HB analysis using 4 complex harmonics reproduced the solution of the fully time-resolved $TD\ \ 128$ analysis nearly 10 times more rapidly than the TD analysis. The HB RANS method has a strong potential of improving utility-scale HAWT design since it enables the use of the NS equations to determine fatigue-inducing and power-reducing loads more accurately than low-fidelity analysis methods and more rapidly than conventional time-domain NS CFD. The high computational efficiency of the HB technology, possibly with the initial support of reliable reduced order modeling, offers the possibility of optimizing the design of HAWT rotors, accurately accounting for complex unsteady flow features.

For VAWTs the assessment was based on the analysis of the periodic flow of the rotor section of a small H-Darrieus rotor working at a near-maximum power tip-speed ratio of 3.3. Although the overall agreement of the HB and TD analyses was fairly good, the comparison of the torque profiles and the power coefficient of the two simulations revealed differences of up to 5 percent. This is due to the high level of stall characterizing the operation of Darrieus rotors at and around peak power conditions which prevents the pseudo-time-marching solution of the HB equations from fully converging. This flow regime type is quite different from that typically encountered in utility-scale HAWT rotors, which experience much smaller stall levels due to effective rotor speed and blade pitch control systems, and whose HB periodic flow analyses thus present fewer numerical difficulties. Nevertheless, the HB and TD VAWT rotor predictions are sufficiently close to consider future use of the HB method for VAWT preliminary design.

For aerodynamic problems charactereized by high stall levels, like Darrieus rotor flows, more research aiming at alleviating the numerical instabilities of the HB solver and improving its convergence properties appears to be needed. Code stabilization techniques previously used to remove this type of instability, such as the *Recursive Projection Method* [49] and the *Proper Orthogonal Decomposition* [50], could be tested also for improving the HB NS technology.

A novel fully coupled MG solution procedure of the compressible RANS and SST turbulence model equations that uses a point-implicit integration of the turbulence equations has been discussed. An important approximation to the integration of the SST equations, valid for low-speed flows, resulting in a partial decoupling of the two SST equations, and yielding higher numerical stability of both steady and HB equations, has also been discussed.

Finally, it is noted that the runtime of HB NS solvers can be substantially further reduced by exploiting the possibility of parallelizing the routine cycles of the HB code looping over the $2N_H + 1$ flow snapshots [51, 39]. This can be viewed as an effective approach to time-parallelizing the solution of periodic flows, an opportunity unavailable in this form in TD codes.

Acknowledgement

This work made use of the facilities of N8 HPC provided and funded by the N8 consortium and EPSRC (Grant No.EP/K000225/1). The Centre is co-ordinated by the Universities of Leeds and Manchester. The authors also acknowledge use of Hartree Centre resources in this work. The STFC Hartree Centre is a collaborative research programme in association with IBM providing High Performance Computing platforms funded by the UK's investment in e-Infrastructure. Dr. F. Balduzzi, Dr. A. Bianchini and Dr. L. Ferrari are acknowledged for providing the FLUENT-based VAWT results reported in this paper.

References

[1] M. Hansen, Aerodynamics of wind turbines, Second edition, Earthscan, London, 2008.

[2] J. Manwell, J. McGowan, A. Rogers, Wind Energy Explained. Theory, Design and Application, John Wiley and Sons Ltd., 2002.

[3] S. Tsalicoglou, S. Barber, N. Cholani, R. Abhari, Effect of Flow Inclination on Wind Turbine Performance, Journal of Engineering for Gas Turbine and Power 134 (12) (2012) 122601.1–122601–8.

[4] M. Brahimi, A. Allet, I. Paraschivoiu, Aerodynamic analysis models for vertical-axis wind turbines, International Journal of Rotating Machinery 21 (1) (1995) 15–21.

[5] E. Amet, T. Maitre, C. Pellone, j.-L. Achard, 2D Numerical Simulations of Blade-Vortex Interaction in a Darrieus Turbine, Journal of Fluids Engineering 131 (2009) 111103.1–111103.15.

[6] C. Simao-Ferreira, A. van Zuijlen, H. Bijl, G. van Bussel, G. van Kuik, Simulating dynamic stall on a two-dimensional vertical-axis wind turbine: verification and validationwith particle image velocimetry data, Wind Energy 13 (2010) 1–17.

[7] M. Hansen, J. Sorensen, S. Voutsinas, N. Sorensen, H. Madsen, State of the art in wind turbine aerodynamics and aeroelasticity, Progress in Aerospace Sciences 42 (2006) 285–330.

[8] P. Jain, Wind Energy Engineering, McGraw-Hill, New York, NY, USA, 2011.

[9] C. Bak, Aerodynamic design of wind turbine rotors, in: W. Gentzsch, U. Harms (Eds.), Advances in wind turbine blade design and materials, Vol. 47 of Energy, Woodhead Publishing, Cambridge, UK, 2013, pp. 59–108.

[10] H. Himmelskamp, Profile investigations of a rotating airscrew, in: PhD Dissertation Goettingen 1945, Report and Translation 832, MAP Voelkenrode, 1947.

[11] M. Campobasso, F. Gigante, J. Drofelnik, Turbulent Unsteady Flow Analysis of Horizontal Axis Wind Turbine Airfoil Aerodynamics Based on the Harmonic Balance Reynolds-Averaged Navier-Stokes Equations, ASME paper GT2014-25559 (June 2014).

[12] H. Madsen, N. Sorensen, S. Schreck, Yaw Aerodynamics Analyzed with Three Codes in Comparison with Experiments, AIAA paper 2003-0519, 41st AIAA Aerospace Sciences Meeting and Exhibit, Reno, Nevada (January 2003).

[13] A. Le Pape, V. Gleize, Improved Navier-Stokes Computations of a Stall-regulated Wind Turbine Using Low Mach Number Preconditioning, AIAA paper 2006-1502, 44th AIAA Aerospace Sciences Meeting and Exhibit, Reno, Nevada (January 2006).

[14] N. Sezer-Uzol, A. Gupta, L. Long, 3D Time-Accurate Inviscid and Viscous cfd Simulations of Wind Turbine Rotor Flow Fields, in: I. Tuncer, U. Guelcat, D. Emerson, K. M. (Eds.) (Eds.), Parallel Computational Fluid Dynamics 2007, Vol. 67 of Lecture Notes in Computational Science and Engineering, Springer-Verlag, 2007, pp. 457–464.

[15] C. Tsalicoglou, S. Jafari, S. Chokani, R. Abhari, Rans computations of

wind turbine near-wake aerodynamics in uniform and yawed inflow, ASME paper GT2013-96034 (June 2013).

[16] A. Iida, K. Kato, A. Mizuno, Numerical Simulation of Unsteady Flow and Aerodynamics Performance of Vertical Axis Wind Turbines with LSE, AIAA paper 78-257, 16th Australian Fluid Mechanics Conference, Gold Coast, Australia (December 2007).

[17] R. Howell, N. Qin, J. Edwards, N. Durrani, Critical issues in the simulation of darrieus wind turbines, Renewable Energy 35 (2010) 412–422.

[18] A. Rossetti, G. Pavesi, Comparison of different numerical approaches to the study of the h-darrieus turbines start-up, Renewable Energy 50 (2013) 7–19.

[19] F. Balduzzi, A. Bianchini, R. Maleci, G. Ferrara, L. Ferrari, Critical issues in the simulation of darrieus wind turbines, Renewable Energy 85 (2016) 419–435.

[20] K. Hall, J. Thomas, W. Clark, Computations of Unsteady Nonlinear Flows in Cascades Using a Harmonic Balance Technique, AIAA Journal 40 (5) (2002) 879–886.

[21] E. van der Weide, A. Gopinath, A. Jameson, Turbomachinery Applications with the Time Spectral Method, AIAA paper 2005-4905, 17th AIAA Computational Fluid Dynamics Conference, Torontp, Ontario, Canada (June 2005).

[22] X. Su, X. Yuan, Implicit Solution of Time-Spectral Method for Periodic Unsteady Flows, International Journal for Numerical Methods in Fluids 63 (7) (2010) 860–876.

[23] A. Da Ronch, A. McCracken, K. Badcock, , M. Widhalm, M. Campobasso, Linear Frequency Domain and Harmonic Balance Predictions of Dynamic Derivatives, Journal of Aircraft 50 (3) (2013) 694–707.

[24] F. Sicot, G. Puigt, M. Montagnac, Block-Jacobi Implicit Algorithms for the Time Spectral Method, AIAA Journal 46 (12) (2008) 3080–3089.

[25] M. A. Woodgate, K. J. Badcock, Implicit Harmonic Balance Solver for Transonic Flows with Forced Motions, AIAA Journal 47 (4) (2009) 893–901.

[26] M. Campobasso, M. Baba-Ahmadi, Analysis of Unsteady Flows Past Horizontal Axis Wind Turbine Airfoils Based on Harmonic Balance Compressible Navier-Stokes Equations with Low-Speed Preconditioning, Journal of Turbomachinery 134 (6).

[27] J. Howison, K. Ekici, Unsteady Analysis of Wind Turbine Flows Using the Harmonic Balance Method, AIAA paper 2013-1107, 51st AIAA Aerospace Sciences Meeting including the New Horizons Forum and Aerospace Exposition, Grapewine (Dallas/Ft. Worth Region), Texas (January 2013).

[28] P. Spalart, S. Allmaras, A one-equation turbulence model for aerodynamic flows, La Recherche Aerospatiale 1 (1994) 5–21.

[29] J. Howison, K. Ekici, Dynamic stall analysis using harmonic balance and correlation based $\gamma - re_\theta$ transition models for wind turbine applications, Wind Energy 18 (2015) 2047–2063.

[30] F. Menter, Two-equation Turbulence-models for Engineering Applications, AIAA Journal 32 (8) (1994) 1598–1605.

[31] J. Vassberg, A. Gopinath, A. Jameson, Revisiting the Vertical-Axis Wind-Turbine Design using Advanced Computational Fluid Dynamics, AIAA paper 2005-47, 43rd AIAA Aerospace Sciences Meeting and Exhibit, Reno, Nevada (January 2005).

[32] D. Wilcox, Reassessment of the Scale-Determining Equation for Advanced Turbulence Models, AIAA Journal 26 (11) (1988) 1299–1310.

[33] W. Jones, B. Launder, The Calculation of Low-Reynolds-Number Phenomena with a Two-Equation Model for Turbulence, International Journal of Heat and Mass Transfer 16 (1973) 1119–1130.

[34] F. Liu, X. Zheng, A Strongly Coupled Time-Marching Method for Solving the Navier-Stokes and $K-\omega$ Turbulence Model Equations with Multigrid, Journal of Computational Physics 128 (2) (1996) 289–300.

[35] F. Lin, F. Sotiropoulos, Strongly-Coupled Multigrid Method for 3-D Incompressible Flows Using Near-Wall Turbulence Closures, Journal of Fluids Engineering 119 (1997) 314–324.

[36] L. Liu, J. Thomas, E. Dowell, P. Attar, K. Hall, A comparison of classical and high dimensional harmonic balance approaches for a Duffing oscillator, Journal of Computational Physics 215 (1) (2006) 298–320.

[37] M. Campobasso, A. Piskopakis, J. Drofelnik, A. Jackson, Turbulent Navier-Stokes Analysis of an Oscillating Wing in a Power-Extraction Regime Using the Shear Stress Transport Turbulence Model, Computers and Fluids 88 (2013) 136–155.

[38] M. Campobasso, J. Drofelnik, Compressible Navier-Stokes analysis of an oscillating wing in a power-extraction regime using efficient low-speed preconditioning, Computers and Fluids 67 (2012) 26–40.

[39] A. Jackson, M. Campobasso, M. Baba-Ahmadi, On the Parallelization of a Harmonic Balance Compressible Navier-Stokes Solver for Wind Turbine Aerodynamics, ASME paper GT2011-45306 (2011).

[40] F. Menter, Zonal Two Equation K-ω Turbulence Models for Aerodynamic Flows, AIAA paper 93-2906, 24th AIAA Fluid Dynamics Conference, Orlando, Florida (July 1993).

[41] N. Melson, D. Sanetrik, H. Atkins, Time-accurate Navier-Stokes Calculations with Multigrid Acceleration, Proc. 6^{th} Copper Mountain Conference on Multigrid Methods (1993) II423–II437.

[42] M. Campobasso, M. Baba-Ahmadi, Ad-hoc Boundary Conditions for CFD Analyses of Turbomachinery Problems with Strong Flow Gradients at Farfield Boundaries, Journal of Turbomachinery 133 (4).

[43] M. Raciti-Castelli, A. Englaro, E. Benini, The Darrieus wind turbine: proposal for a new performance prediction model based on cfd, Energy 36 (2011) 4919–4934.

[44] M. Raciti-Castelli, G. Pavesi, L. Battisti, E. Benini, G. Ardizzon, Modeling strategy and numerical validation for a Darrieus vertical axis micro-wind turbine, ASME paper IMECE-2010-39548, aSME 2010 International Mechanical Engineering Congress and Exposition, Vancouver, Canada (November 2010).

[45] F. Balduzzi, A. Bianchini, F. Gigante, G. Ferrara, M. Campobasso, L. Ferrari, Parametric and Comparative Assessment of Navier-Stokes CFD Methodologies for Darrieus Wind Turbine Performance Analysis, ASME paper GT2015-42663, aSME Turbo Expo 2015, Gas turbine Technical Conference and Exposition, Montreal, Canada (June 2015).

[46] Ansys, Fluent theory guide, Tech. Rep. release 14.5 (2013).

[47] M. Campobasso, M. Yan, J. Drofelnik, A. Piskopakis, M. Caboni, Compressible Reynolds-Avergaed Navier-Stokes Analysis of wind Turbine Turbulent Flows Using a Fully Coupled Low-Speed Preconditioned Multigrid Solver, ASME paper GT2014-25562 (June 2014).

[48] M. Campobasso, M. Giles, Effects of flow instabilities on the linear analysis of turbomachinery aeroelasticity, Journal of Propulsion and Power 19 (2) (2003) 250–259.

[49] M. S. Campobasso, M. B. Giles, Stabilization of Linear Flow Solver for Turbomachinery Aeroelasticity Using Recursive Projection Method, AIAA Journal 42 (9) (2004) 1765–1774.

[50] K. Ekici, K. Hall, H. Huang, J. Thomas, Stabilization of Explicit Flow Solvers Using a Proper-Orthogonal-Decomposition Technique, AIAA Journal 51 (5) (2013) 1095–1104.

[51] Z. Yang, D. Mavriplis, Time Spectral Method for Periodic and Quasi-Periodic Unsteady Computations on Unstructured Meshes, AIAA paper 2010-5034, 40th Fluid Dynamics Conference and Exhibit, Chicago, Illinois (June-July 2010).